

Version 1.1, Submitted to PASP

Astrometric calibration and performance of the Dark Energy Camera

G. M. Bernstein¹, R. Armstrong², A. A. Plazas³, A. R. Walker⁴, T. M. C. Abbott⁴, S. Allam⁵,
K. Bechtol⁶, A. Benoit-Lévy^{7,8,9}, D. Brooks⁸, D. L. Burke^{10,11}, A. Carnero Rosell^{12,13},
M. Carrasco Kind^{14,15}, J. Carretero¹⁶, C. E. Cunha¹⁰, L. N. da Costa^{12,13}, D. L. DePoy¹⁷,
S. Desai¹⁸, H. T. Diehl⁵, T. F. Eifler³, E. Fernandez¹⁶, P. Fosalba¹⁹, J. Frieman^{5,20},
J. García-Bellido²¹, D. W. Gerdes^{22,23}, D. Gruen^{10,11}, R. A. Gruendl^{14,15}, J. Gschwend^{12,13},
G. Gutierrez⁵, K. Honscheid^{24,25}, D. J. James^{26,4}, S. Kent^{5,20}, E. Krause¹⁰, K. Kuehn²⁷,
N. Kuropatkin⁵, T. S. Li^{5,17}, M. A. G. Maia^{12,13}, M. March¹, J. L. Marshall¹⁷, F. Menanteau^{14,15},
R. Miquel^{28,16}, R. L. C. Ogando^{12,13}, K. Reil¹¹, A. Roodman^{10,11}, E. S. Rykoff^{10,11}, E. Sanchez²⁹,
V. Scarpine⁵, R. Schindler¹¹, M. Schubnell²³, I. Sevilla-Noarbe²⁹, M. Smith³⁰, R. C. Smith⁴,
M. Soares-Santos⁵, F. Sobreira^{12,31}, E. Suchyta³², M. E. C. Swanson¹⁵, G. Tarle²³

(DES Collaboration)

-
- ¹Department of Physics and Astronomy, University of Pennsylvania, Philadelphia, PA 19104, USA
- ²Department of Astrophysical Sciences, Princeton University, Peyton Hall, Princeton, NJ 08544, USA
- ³Jet Propulsion Laboratory, California Institute of Technology, 4800 Oak Grove Dr., Pasadena, CA 91109, USA
- ⁴Cerro Tololo Inter-American Observatory, National Optical Astronomy Observatory, Casilla 603, La Serena, Chile
- ⁵Fermi National Accelerator Laboratory, P. O. Box 500, Batavia, IL 60510, USA
- ⁶LSST, 933 North Cherry Avenue, Tucson, AZ 85721, USA
- ⁷CNRS, UMR 7095, Institut d’Astrophysique de Paris, F-75014, Paris, France
- ⁸Department of Physics & Astronomy, University College London, Gower Street, London, WC1E 6BT, UK
- ⁹Sorbonne Universités, UPMC Univ Paris 06, UMR 7095, Institut d’Astrophysique de Paris, F-75014, Paris, France
- ¹⁰Kavli Institute for Particle Astrophysics & Cosmology, P. O. Box 2450, Stanford University, Stanford, CA 94305, USA
- ¹¹SLAC National Accelerator Laboratory, Menlo Park, CA 94025, USA
- ¹²Laboratório Interinstitucional de e-Astronomia - LIneA, Rua Gal. José Cristino 77, Rio de Janeiro, RJ - 20921-400, Brazil
- ¹³Observatório Nacional, Rua Gal. José Cristino 77, Rio de Janeiro, RJ - 20921-400, Brazil
- ¹⁴Department of Astronomy, University of Illinois, 1002 W. Green Street, Urbana, IL 61801, USA
- ¹⁵National Center for Supercomputing Applications, 1205 West Clark St., Urbana, IL 61801, USA
- ¹⁶Institut de Física d’Altes Energies (IFAE), The Barcelona Institute of Science and Technology, Campus UAB, 08193 Bellaterra (Barcelona) Spain
- ¹⁷George P. and Cynthia Woods Mitchell Institute for Fundamental Physics and Astronomy, and Department of Physics and Astronomy, Texas A&M University, College Station, TX 77843, USA
- ¹⁸Department of Physics, IIT Hyderabad, Kandi, Telangana 502285, India
- ¹⁹Institut de Ciències de l’Espai, IEEC-CSIC, Campus UAB, Carrer de Can Magrans, s/n, 08193 Bellaterra, Barcelona, Spain
- ²⁰Kavli Institute for Cosmological Physics, University of Chicago, Chicago, IL 60637, USA
- ²¹Instituto de Física Teórica UAM/CSIC, Universidad Autónoma de Madrid, 28049 Madrid, Spain
- ²²Department of Astronomy, University of Michigan, Ann Arbor, MI 48109, USA
- ²³Department of Physics, University of Michigan, Ann Arbor, MI 48109, USA
- ²⁴Center for Cosmology and Astro-Particle Physics, The Ohio State University, Columbus, OH 43210, USA
- ²⁵Department of Physics, The Ohio State University, Columbus, OH 43210, USA
- ²⁶Astronomy Department, University of Washington, Box 351580, Seattle, WA 98195, USA
- ²⁷Australian Astronomical Observatory, North Ryde, NSW 2113, Australia
- ²⁸Institució Catalana de Recerca i Estudis Avançats, E-08010 Barcelona, Spain
- ²⁹Centro de Investigaciones Energéticas, Medioambientales y Tecnológicas (CIEMAT), Madrid, Spain

ABSTRACT

We characterize the ability of the Dark Energy Camera (DECam) to perform relative astrometry across its 500 Mpix, 3-deg² science field of view, and across 4 years of operation. This is done using internal comparisons of $\sim 4 \times 10^7$ measurements of high- S/N stellar images obtained in repeat visits to fields of moderate stellar density, with the telescope dithered to move the sources around the array. An empirical astrometric model includes terms for: optical distortions; stray electric fields in the CCD detectors; chromatic terms in the instrumental and atmospheric optics; shifts in CCD relative positions of up to $\approx 10 \mu\text{m}$ when the DECam temperature cycles; and low-order distortions to each exposure from changes in atmospheric refraction and telescope alignment. Errors in this astrometric model are dominated by stochastic variations with typical amplitudes of 10–30 mas (in a 30 s exposure) and 5'–10' coherence length, plausibly attributed to Kolmogorov-spectrum atmospheric turbulence. The size of these atmospheric distortions is not closely related to the seeing. Given an astrometric reference catalog at density $\approx 0.7 \text{ arcmin}^{-2}$, *e.g.* from Gaia, the typical atmospheric distortions can be interpolated to ≈ 7 mas RMS accuracy (for 30 s exposures) with 1' coherence length in for residual errors. Remaining detectable error contributors are 2–4 mas RMS from unmodelled stray electric fields in the devices, and another 2–4 mas RMS from focal plane shifts between camera thermal cycles. Thus the astrometric solution for a single DECam exposure is accurate to 3–6 mas (≈ 0.02 pixels, or ≈ 300 nm) on the focal plane, plus the stochastic atmospheric distortion.

Subject headings: astrometry—atmospheric effects—methods: data analysis—instrumentation: detectors

Contents

1	Introduction	5
2	Methods	6
2.1	Terminology	7

³⁰School of Physics and Astronomy, University of Southampton, Southampton, SO17 1BJ, UK

³¹Universidade Federal do ABC, Centro de Ciências Naturais e Humanas, Av. dos Estados, 5001, Santo André, SP, Brazil, 09210-580

³²Computer Science and Mathematics Division, Oak Ridge National Laboratory, Oak Ridge, TN 37831

2.2	Available maps	8
2.3	Degeneracies	10
2.3.1	Shift	10
2.3.2	Color shift	10
2.3.3	Linear	11
2.3.4	Colony collapse disorder	11
2.3.5	Exposure/instrument trades	11
2.3.6	Unconstrained parameters	12
2.4	Algorithms	12
2.4.1	χ^2 minimization	12
2.4.2	Outlier rejection	13
2.4.3	Procedure	14
2.5	Performance	15
3	Input data	15
4	The DECam astrometric model	16
4.1	Tree rings	18
4.2	Edges	20
4.3	Optics polynomials	21
4.4	CCD shifts	23
4.5	Lateral color	23
4.6	Exposure solution	24
4.7	Differential chromatic refraction	24
5	Unmodelled distortions	26
6	Stochastic errors	28
6.1	Atmospheric turbulence	28
6.2	Behavior of the stochastic component	30
7	Solution stability	32
8	Interpolation schemes	36
9	Conclusions	39
A	E/B vector field correlation functions	43

1. Introduction

The Dark Energy Camera (Flaugher et al. 2015, DECam) is one member of a new generation of high-throughput imagers combining large field of view (3 deg² for DECam) with large telescope aperture (the 4-meter Blanco telescope). In the post-Gaia era (Gaia Collaboration 2016), when positions, proper motions, and parallaxes are expected to be available with < 1 milliarcsecond (mas) accuracy for the 10^9 stars with magnitude $G \lesssim 20$, what need do we have for accurate astrometry from these large ground-based cameras? There remain strong scientific motivations to obtain the most accurate possible positions for sources fainter than Gaia’s limit, for transient sources, and for solar-system bodies. Ideally these general-purpose, large-format imagers would be capable of obtaining astrometric measurements limited by the unavoidable shot noise and atmospheric fluctuations. Motivation and practice of astrometry from large-format ground-based CCD cameras have been discussed by Anderson et al. (2006), Platais, Wyse, & Zacharias (2006), Bouy et al. (2013), and Magnier et al. (2016), among others. Accurate astrometry underlies many of the science goals of the *Large Synoptic Survey Telescope (LSST)* now under construction (LSST Collaboration 2009).

In addition, one of the motivators for construction of DECam is measurement of weak gravitational lensing distortions of galaxies. Success in this pursuit requires the ability to register multiple exposures of every galaxy to an accuracy of ≈ 10 mas or better—otherwise the blur induced by mis-registration in combining images could be mistaken for a coherent weak-lensing distortion. Searches for transient sources also benefit from precise image registration to improve subtraction of static sources.

One thing we do *not* need our wide-field imagers to do is determine absolute positions, since the preliminary Gaia catalogs are sufficiently dense to yield thousands of stars in the spatial and dynamic-range overlap between Gaia and most DECam exposures. These suffice to determine the absolute pointing and any low-order astrometric distortion terms across the DECam field of view. In this work we therefore focus on establishing *relative* astrometry with DECam on scales $\lesssim 1^\circ$. Indeed one might ask why to bother at all with the effort making an astrometric model for DECam instead of simply interpolating all positional errors from Gaia stars. First, many of the detector-level effects occur on angular scales too small for Gaia stars to sample. Second, if our model removes discontinuities in the astrometric errors between CCDs, we can interpolate using reference stars from the whole field rather than being confined to those on a single device. Furthermore the Gaia proper motion catalog is not yet available, so the reference catalog is not yet at mas accuracy. Lastly many DECam exposures may have dynamic range which does not overlap well with the Gaia catalog.

In Section 2 we describe our method of deriving the DECam astrometric map and its error properties by forcing internal agreement amongst stellar positions in a series of offset exposures of rich star fields. In Sections 3, 4, and 5 we describe the data used to characterize DECam astrometry, the model applied to it, and the *static* residuals to this model, *i.e.* those which repeat from exposure to exposure. Section 6 characterizes the *stochastic* residuals, *i.e.* those uncorrelated between consecutive exposures and presumably due to atmospheric fluctuations. Section 7 characterizes the changes in the astrometric model from night to night and over the first 4 years of DECam observations. Section 8 investigates how much of the stochastic distortion can be removed

by interpolation from a set of reference stars of a given density.

Our goal will be to model any astrometric distortion that contributes more than ≈ 1 mas RMS error that is correlated between stars separated by $> 10''$. To put this scale in context, note that the mean scale of a $15 \mu\text{m}$ DECam pixel is 264 mas, so 1 mas corresponds to 0.004 pixel = 60 nm, or about 100 atoms in the silicon lattice. The DECam science array consists of 62 deep-depletion CCDs, each 2048×4096 pixels, and the array spans a roughly hexagonal area of diameter 2° . Thus 1 mas is 1.4 parts in 10^7 of the DECam field of view. Scale changes due to stellar aberration, air pressure variations, and atmospheric refraction are far larger than this, so we will clearly need to allow each exposure an independent overall linear transformation across the FOV to approach mas accuracy. Indeed the *nonlinear* portion of atmospheric refraction is expected to have peak-to-peak amplitude of $(14 \text{ mas}) \times \sec^2 z \tan z$ across the DECam FOV (where z is the zenith angle), so we must allow at least quadratic freedom to our solution atop any static instrumental model.

RMS positional errors reported in this paper refer to the sum of E-W and N-S components, unless noted otherwise.

2. Methods

The astrometric solution for DECam is a parametric model for the celestial (world) coordinates $\mathbf{x}^w = (x^w, y^w)$ of an object given its observed pixel coordinates $\mathbf{x}^p = (x^p, y^p)$ and some set of observing circumstances C , which might include the object’s color c , plus discrete variables such as the date, exposure, filter, and individual CCD on which the measurement was obtained. The solution is found by straightforward χ^2 -minimization over the values of the model parameters $\boldsymbol{\pi}$. The index i ranges over all position measurements used to constrain the solution, and we assume a measurement error σ_i^p that is the same for both positional components of \mathbf{x}_i^p . We index the distinct objects on the sky by α , let α_i be the object targeted by measurement i , and denote by $i \in \alpha$ the subset of measurements with $\alpha_i = \alpha$. We define

$$\chi^2 \equiv \sum_i w_i |\mathbf{x}^w(\mathbf{x}_i^p, C_i, \boldsymbol{\pi}) - \bar{\mathbf{x}}_{\alpha_i}|^2 \quad (1)$$

$$\bar{\mathbf{x}}_{\alpha} \equiv \frac{\sum_{i \in \alpha} w_i \mathbf{x}^w(\mathbf{x}_i^p, C_i, \boldsymbol{\pi})}{\sum_{i \in \alpha} w_i} \quad (2)$$

$$w_i^{-1} = (\sigma_i^2 + \sigma_{\text{sys}}^2) \left| \frac{d\mathbf{x}^w}{d\mathbf{x}^p} \right|_i. \quad (3)$$

In (3) we introduce σ_{sys} to prevent very high weights from being assigned to high- S/N measurements. We may consider σ_{sys} to represent the expected stochastic position errors beyond those arising from image noise that are included in σ_i . In practice we find that stochastic atmospheric distortions dominate the astrometric residuals, so we set σ_{sys} near the typical RMS atmospheric distortion in our data (~ 10 mas, *cf.* Sec 6). This fairly arbitrary choice appropriately equalizes the weights assigned to individual measurements, but it does mean that our final χ^2 values should not be expected to follow a χ^2 distribution—it serves only as the quantity used to optimize $\boldsymbol{\pi}$.

Note that measurements from DECam can be freely mixed with other instruments’ position measurements in Equation (1). *Internal* constraints—that multiple DECam observations of a source

yield the same world coordinates—are combined with *external* constraints that DECam match a source of *a priori* assigned world coordinates of these objects. We denote as a **reference catalog** any set of measured positions that are independent of $\boldsymbol{\pi}$, *i.e.* the function $\mathbf{x}^w(\mathbf{x}^p)$ is simply the identity, and the reference catalog directly specifies \mathbf{x}_i^w and errors σ_i^w .

Our strategy for DECam calibration is to produce very strong internal constraints by taking a series of ≈ 20 consecutive exposures of fields at modest Galactic latitudes, where stellar sources are abundant but not crowded. The pointings of these exposures are shifted by anywhere from $10''$ to the FOV diameter, so that a given star is imaged at many places on the array. In this scheme the reference catalog serves mainly to break degeneracies in overall position and linear scaling of the astrometric map (see Section 2.3). These sequences of exposures are called **star flats** (since they are also used to calibrate photometric response). Since DECam was installed in 2012, star flat sequences in all filters have been executed several times per year, usually during bright time. These data, described in Table 1, are the ones used in this paper to derive the DECam astrometric model.

In the remainder of this section we will detail the algorithmic and coding choices made in defining the maps $\mathbf{x}^w(\mathbf{x}^p)$ and in the minimization of χ^2 . These choices are realized in C++ code with an executable program called WCSFIT. A reader uninterested in the implementation details can skip to Section 4.

2.1. Terminology

We adopt the following terminology:

- A **pixel map** is a function $\mathbf{x}^w(\mathbf{x}^p)$ giving the transformation from detector coordinates to world coordinates. These maps are realized by compounding several functions, each of which may also be referred to as a pixel map.
- A **detection** is a single measurement of a stellar position, which as noted is described by pixel coordinates \mathbf{x}_i^p and an associated uncertainty σ_i .
- A **device** is a region of the focal plane over which we expect to have a continuous pixel map, *i.e.* one of the CCDs in the DECam focal plane. Every detection belongs to exactly one device.
- An **exposure** comprises all the detections obtained simultaneously during one opening of the shutter. The exposure number is essentially our discrete time variable.
- An **extension** comprises the detections made on a single device in a single exposure.¹ WCSFIT allows each extension to be assigned its own pixel map, which will be a continuous function. Every detection belongs to exactly one extension.

¹The name arises from each device’s detection list typically appearing in a distinct binary table extension of a FITS-format file.

- A **catalog** is the collection of all detections from a single exposure, *i.e.* the union of the extensions from all the devices in use for that exposure.
- A **band** labels the filter used in the observation. Every exposure has exactly one band.
- An **epoch** labels a range of dates over which the physical configuration of the instrument, aside from filter choice and the pointing of the telescope, is considered (astrometrically) invariant. Every exposure belongs to exactly one epoch.
- An **instrument** is a given configuration of the camera for which we expect the instrumental optics to yield an invariant astrometric solution. In our analyses an instrument is specified by a combination of band and epoch. Every exposure is associated with exactly one instrument. This is the same definition as used in SCAMP (Bertin 2006), the public code commonly used for astrometric solutions.
- A **field** is a region of the sky holding the detections from a collection of exposures. Every exposure is associated with exactly one field. Each field f has a central right ascension and declination (α_f, δ_f) . The world coordinates \mathbf{x}^w are defined to be in the gnomonic projection of the sky about the field center.
- A **match**, sometimes called an **object**, comprises all the detections that correspond to a common celestial source and are therefore expected to have common true \mathbf{x}^w .² In this astrometric study we will make use only of stellar sources, so a match is simply a star. We only allow matches to be constructed between detections in a common field.
- A **reference catalog** is an extension for which there are no free parameters in the map to world coordinates, for example the list of Gaia stars for a given field. The distinction between devices, instruments, etc. is irrelevant for these, and we can consider all sources of reference information as belonging to a common catalog.

As detailed in Section 2.2, WCSFIT allows the pixel map for extension k to be composed of a sequence of “atomic” transformations. Following SCAMP we will divide the overall pixel map applied to a given extension into an *instrumental* map followed by an *exposure* map. The former goes from pixel coordinates of each device to an intermediate system of a gnomonic projection about the telescope optic axis, and is taken to be constant within an epoch. The exposure map is continuous across the field of view and takes independent parameters for each exposure.

2.2. Available maps

We must specify a functional form (and free parameters) for a map $\mathbf{m}_k(\mathbf{x}^p, c)$ from pixels to world coordinates for each extension k . Here c is the object color, and the other elements of the observational circumstances C are specified by the extension index. WCSFIT allows each map \mathbf{m}_k to

²WCSFIT does not yet consider proper motions of sources.

be specified as the composition of a series of $j = 1, 2, \dots, N_k$ “atomic” coordinate transformations $\mathbf{m}_k^{(i)}$:

$$\mathbf{x}^{(0)} = \mathbf{x}^p, \tag{4}$$

$$\mathbf{x}^{(i)} = \mathbf{m}_k^{(i)}(\mathbf{x}^{(i-1)}) \tag{5}$$

$$\mathbf{x}^w = \mathbf{x}^{(N_k)}. \tag{6}$$

We will generically refer to the input of each transformation $\mathbf{m}_k^{(i)}$ as its “pixel” coordinates and the output as its “world” coordinates, even though the intermediate variables are in fact neither. In our application, the chain of component maps is divided into those of the instrument solution followed by those of the exposure solution.

WCSFIT follows the definitions in Section 2.1 by making each coordinate transformation or element thereof an instance of an abstract C++ base class `PixelMap`. Each has a `type`, a unique `name` string, and has a number ≥ 0 of free parameters controlling its actions. `PixelMap` instances can be (de-)serialized (from) to ASCII files in YAML format, easily read or written by humans. The WCSFIT user specifies the transformations to be fit to the data by giving the program such a YAML file as input—the parameters are assigned default starting values if none are specified. Anywhere that the strings `BAND`, `INSTRUMENT`, `EPOCH`, or `DEVICE` appear in these input files they are replaced with the values appropriate to the extension, allowing a generic model to be specified compactly. The WCSFIT user can also specify the names of any `PixelMaps` whose parameters should be held fixed at their input values. The primary output of WCSFIT is another YAML file specifying all of the maps and their best-fit parameters.

The types of `PixelMaps` available for use are:

- The `Identity` map, which leaves \mathbf{x} unchanged, and has no free parameters.
- `Constant` maps have $\mathbf{x}^w = \mathbf{x}^p + \mathbf{x}_0$, with the two components of \mathbf{x}_0 as parameters.
- `Linear` maps have $\mathbf{x}^w = A\mathbf{x}^p + \mathbf{x}_0$, with six parameters in \mathbf{x}_0 and the components of the matrix A .
- `Polynomial` maps have their free parameters as the coefficients of two polynomials of specified degrees d_x and d_y in the \mathbf{x}^p components that produce x^w and y^w , respectively.
- `Template` maps apply transformations based on lookup tables. One has the option of x, y, or radial transformations:

$$x^w = x^p + sf(x^p), \tag{7}$$

$$y^w = y^p + sf(y^p), \text{ or} \tag{8}$$

$$\mathbf{x}^w = \mathbf{x}^p + s \frac{\mathbf{x}^p - \mathbf{x}_c}{|\mathbf{x}^p - \mathbf{x}_c|} f(|\mathbf{x}^p - \mathbf{x}_c|), \tag{9}$$

The first two cases each operate in only a single cartesian direction. In the third (radial) case, the center \mathbf{x}_c of the distortion is specified. There is a single free parameter, the scaling parameter s . The template function f is defined as linear interpolation between values v_j at nodes $a_0 + j \Delta a$ for $0 \leq j \leq N$.

- **Piecewise** maps are functionally identical to the **Template** map, except that the nodal values v_j are the free parameters, and the scaling is fixed to $s = 1$.
- A **Color** term is defined by

$$\mathbf{x}^w = \mathbf{x}^p + (c - c_{\text{ref}}) [\mathbf{m}(\mathbf{x}^p) - \mathbf{x}^p] \quad (10)$$

where c_{ref} is a reference color and \mathbf{m} is an instance of any of the above forms of transformation. The parameters of the **Color** map are those of the map it scales.

- **Reprojection** maps have no free parameters: they merely move coordinates from one projection of the sphere to another.
- **Composite** maps realize Equations (4)–(6) for a specified sequence of any of maps (including other **Composite** maps). The parameters of the composite are the concatenation of those of the component maps.

A **PixelMap**, in combination with a specification of the projection in which the \mathbf{x}^w maps to the celestial sphere, forms a complete world coordinate system (WCS).

2.3. Degeneracies

When minimizing χ^2 we must be aware of degeneracies whereby $\boldsymbol{\pi}$ can change while χ^2 is invariant. Such degeneracies will lead to (near-)zero singular values in the normal matrix \mathbf{A} used in the solution for $\boldsymbol{\pi}$ (Section 4), and failures or inaccuracies in its inversion. There are several such landmines which we must clearly avoid. We will assume in this discussion that the astrometric model for each extension is a device-based instrumental function $\mathbf{x}^T = D(\mathbf{x}^p)$ from pixel to “telescope” coordinates, followed with an exposure-based function $\mathbf{x}^w = E(\mathbf{x}^T)$.

2.3.1. Shift

The simplest degeneracy is a shift in all stellar positions, $E \rightarrow E + \Delta\mathbf{x}$ for every exposure (in the flat-sky limit; more generally the degeneracy is a rotation of the celestial sphere). Each star α has its derived sky position $\bar{\mathbf{x}}_\alpha^w$ shifted as well, but since χ^2 is differential, there is no effect on χ^2 . This degeneracy is broken by having a reference catalog for which \mathbf{x}^w is fixed. The reference catalogs does not need to be very dense or precise to break this degeneracy.

2.3.2. Color shift

A color-dependent shift $E \rightarrow E + c\Delta\mathbf{x}$ is also undetectable in the differential χ^2 . This degeneracy is broken if colors are known for reference stars over a finite range of color.

2.3.3. Linear

In the flat-sky limit consider the case where the exposure component for exposure k is an affine transformation $E_k = \mathbf{A}_k \mathbf{x}^T + \mathbf{x}_k$ with linear rescaling \mathbf{A}_k and offset \mathbf{x}_k , the latter corresponding to the pointing of the telescope at exposure k . An object α with world coordinates \mathbf{x}_α^w will be observed at telescope coordinate $\mathbf{x}_{k\alpha}^T = \mathbf{A}^{-1} (\mathbf{x}_\alpha^w - \mathbf{x}_k)$. For any non-degenerate matrix \mathbf{B} there is an alternative solution

$$\mathbf{A}_k \rightarrow \mathbf{B}\mathbf{A}_k \tag{11}$$

$$\mathbf{x}_k \rightarrow \mathbf{B}^{-1}\mathbf{x}_k \tag{12}$$

$$\mathbf{x}_\alpha^w \rightarrow \mathbf{B}\mathbf{x}_\alpha^w \tag{13}$$

which leaves χ^2 unchanged. This degeneracy is also broken by the existence of a sample of reference stars. There is also a color-dependent variant of this degeneracy.

If the exposure solution E_k has freedom to be altered by some global polynomial function B of order n , then there is generalization of this degeneracy in which each E_k is shifted by a polynomial of order $n-1$. Again the solution is to have a reference catalog of even modest density and accuracy.

2.3.4. Colony collapse disorder

WCSFIT is accelerated by calculating the weight of each observation in Equation (3) just once at the start of fitting, using the determinant of the starting WCS system to convert the pixel errors into world coordinate errors. This opens the door to a pseudo-degeneracy in which all output \mathbf{x}^w values are scaled by some matrix \mathbf{B} , sending $\chi^2 \rightarrow |\mathbf{B}|\chi^2$. If $|\mathbf{B}| \rightarrow 0$, the solution appears to approach perfection while collapsing the output map. This is countered by an increase in χ^2 contributed by the reference stars, which are not collapsing; but if the total weight of the reference stars is too low, the solution will tend toward collapse. The collapse becomes complete if the reference stars are then flagged as outliers and removed by our σ -clipping step. WCSFIT includes a parameter to scale the weights of the reference catalogs, which can be used to prevent this collapse solution if the reference catalog is sparse.

2.3.5. Exposure/instrument trades

For any map F , the transformations

$$E_k \rightarrow E_k F \tag{14}$$

$$D \rightarrow F^{-1} D \tag{15}$$

clearly leaves χ^2 and all \mathbf{x}^w values invariant. If the functional forms being used for E and D admit such a transformation, then the solution is degenerate. The WCSFIT code searches for cases where multiple `Constant`, `Linear`, or `Polynomial` atomic map elements are composited into any exposures' pixel maps and are hence able to trade their terms. This degeneracy can be broken by

setting one of the exposure maps E_k to the `Identity` map. WCSFIT will do this automatically if the user’s configuration leaves such degeneracies in place.

2.3.6. Unconstrained parameters

Map parameters are of course degenerate if there are no stellar observations being affected by them—*e.g.* if a given exposure did not generate any matched detections, or they have all been removed as outliers, then the parameters of the exposure solution are unconstrained.

WCSFIT checks the normal matrix \mathbf{A} for null rows that arise when a parameter does not act on any observations. In this case the diagonal element on this row is set to unity, which stabilizes the matrix inversion and freezes this (irrelevant) parameter in further iterations.

More troublesome is the case where there are a small but non-zero number of observations on an exposure, too few to constrain the model, so that \mathbf{A} is degenerate but without null rows. In this case WCSFIT will fail the attempt to do a Cholesky decomposition of the non-positive-definite \mathbf{A} . In this case WCSFIT will perform a singular value decomposition of \mathbf{A} , report to the user which parameters are associated with near-null singular values, then quit.

2.4. Algorithms

The WCSFIT software suite assumes that we are already in possession of an initial WCS for each extension of sufficient accuracy to allow unambiguous matching of common detections of a source. SCAMP is routinely run on each DES exposure to generate this starting WCS, with accuracy of $< 1''$ relative to Gaia or other reference catalog.

2.4.1. χ^2 minimization

Another benefit of having a good starting WCS for each exposure is that we can initialize parameters of the maps that are defaulted on input by fitting them to the starting WCS—WCSFIT generates set of pseudo-detections on a grid of \mathbf{x}^p spanning the device, and fits them to a pseudo-reference catalog holding the \mathbf{x}^w positions to which the pixel positions are mapped by the WCS.

The algorithm for minimization of χ^2 assumes that the minimizing solution is close to the starting solution, *i.e.* we are doing fine tuning after SCAMP has done the work of bringing us close. The positions are close to linear in the parameters, so the χ^2 value should be close to the usual

quadratic form

$$\chi^2 \approx \chi^2(\boldsymbol{\pi}_0) + 2\mathbf{b} \cdot \Delta\boldsymbol{\pi} + \Delta\boldsymbol{\pi} \cdot \mathbf{A} \cdot \Delta\boldsymbol{\pi}, \quad (16)$$

$$b_\mu \equiv \frac{1}{2} \frac{\partial \chi^2}{\partial \pi_\mu} = \sum_i w_i (\mathbf{x}^w(\mathbf{x}_i^p, \boldsymbol{\pi}_0) - \bar{\mathbf{x}}_{\alpha_i}) \cdot \left(\frac{\partial \mathbf{x}^w(\mathbf{x}_i^p, \boldsymbol{\pi})}{\partial \pi_\mu} - \frac{\partial \bar{\mathbf{x}}_{\alpha_i}}{\partial \pi_\mu} \right) \quad (17)$$

$$A_{\mu\nu} \equiv \left(\frac{\partial \mathbf{x}^w(\mathbf{x}_i^p, \boldsymbol{\pi})}{\partial \pi_\mu} - \frac{\partial \bar{\mathbf{x}}_{\alpha_i}}{\partial \pi_\mu} \right) \cdot \left(\frac{\partial \mathbf{x}^w(\mathbf{x}_i^p, \boldsymbol{\pi})}{\partial \pi_\nu} - \frac{\partial \bar{\mathbf{x}}_{\alpha_i}}{\partial \pi_\nu} \right). \quad (18)$$

Note that the weights w_i are being assumed independent of $\boldsymbol{\pi}$, *i.e.* the world-coordinate errors σ_i^w of each exposure are held fixed at the values implied by the starting WCS. Also note that WCSFIT does not treat the true positions \mathbf{x}_α^w of the sources as free parameters. Instead the dependence of the mean of the measurements $\bar{\mathbf{x}}_\alpha$ upon the parameters is propagated directly into the normal equation.

The calculation of \mathbf{b} and \mathbf{A} is the most computationally intensive part of WCSFIT. The summation for matches is distributed across cores using OPENMP calls. Each match is dependent upon the limited subset of the parameters $\boldsymbol{\pi}$ which appear in the pixel maps for the extensions in which the object is observed, hence the updates to \mathbf{A} are sparse, though the final matrix is dense.

WCSFIT first attempts the Newton iteration

$$\boldsymbol{\pi} \rightarrow \boldsymbol{\pi} - \mathbf{A}^{-1}\mathbf{b}. \quad (19)$$

The solution time scales as the cube of the number of free parameters, and is executed using a multithreaded Cholesky decomposition after preconditioning \mathbf{A} to have unit diagonal elements. Despite the cubic scaling, this step is usually faster than the calculation of the normal matrix. If the decomposition fails due to a non-positive-definite \mathbf{A} , WCSFIT performs a singular-value decomposition on \mathbf{A} and informs the user which parameters dominate the degenerate vectors.

The Newton step is iterated until χ^2 no longer decreases by more than a chosen fraction. Should χ^2 increase during an iteration, or fail to converge within a selected number of steps, then the minimization process is re-started using a Levenberg-Marquart algorithm based on the implementation by [Press et al. \(2003\)](#).

2.4.2. Outlier rejection

The WCSFIT solutions must be robust to astrometric measurements perturbed by unrecognized cosmic rays or defects on the stellar images, and by stars with proper motion or binary partners which alter the photocenter by amounts exceeding measurement errors. We do not at this time fit for proper motion or parallax within WCSFIT.

Outlier rejection is done using standard σ -clipping algorithms. A clipping threshold t is specified at input. After each χ^2 minimization, a rejection threshold is set at $t\sqrt{\chi^2/\text{DOF}}$. Detections whose residual to the fit (in units of σ) exceeds the threshold are discarded. At most one outlier per match is discarded at each clipping iteration.

Outlier clipping is alternated with χ^2 minimization until the clipping step no longer reduces the χ^2 per degree of freedom by a significant amount.

2.4.3. Procedure

The steps in the astrometric solution process are as follows:

1. A preparatory Python program reads an input YAML configuration file specifying the desired input catalog files, plus the definitions of the fields, epochs, and instruments. It then collects from all the catalogs and their headers any information necessary to construct tables of extensions, devices, exposures, and instruments. This includes extracting the serialized starting WCS, usually as produced by SCAMP and stored in the headers of the FITS catalog extensions.
2. A second preparatory program reads all the detections from the input catalogs, applying any desired cuts for S/N and stellarity, and then runs a standard friends-of-friends algorithm to identify all matching detections. Any match that includes multiple detections from the same exposure is discarded. The id's of all groups of matching detections are then stored in another FITS table.
3. WCSFIT starts by ingesting the input FITS tables and creating the structures defining instruments, devices, exposures, and extensions.
4. The YAML file specifying the pixel maps to be applied to each extension is parsed, and a `PixelMap` is created with specified or defaulted parameters. Any of the map elements may have its parameters frozen by the user, the remainder are the free parameters of our model.
5. WCSFIT checks the map configuration for degeneracies: is there reference catalog in each field? Are there any exposure/instrument degeneracies? If so, WCSFIT will attempt to break the degeneracies by setting one or more exposures' maps to `Identity`.
6. All exposures in a field are reprojected to a common gnomonic system about the field center.
7. Any parameters of `PixelMaps` that were set to defaults have their values set by a least-squares fit to the starting WCS. Any degeneracies halt the program.
8. The \mathbf{x}_i^p and σ_i^p of all detections that are part of useful matches are extracted from their source catalogs. For any detections whose maps include color terms, we require a measurement from a color catalog to be matched to the same object. The color catalog is read at this point.
9. A requested fraction of the matches are excluded from the fit at random. These reserved matches can be used later to validate the fit.
10. Any exposures containing insufficient detections are removed from the fit.

11. The iteration between χ^2 minimization and σ -clipping begins. At each iteration, \mathbf{A} is checked for null rows as noted in Section 2.3, which are altered so as to freeze the associated parameter. If \mathbf{A} is not positive-definite, WCSFIT reports the nature of the associated degenerate parameters, then exits.
12. The best-fit astrometric model is written to an output YAML file.
13. After completion of the fit, the best-fit map is applied to both the fit and reserved matches. The σ -clipping algorithm is applied iteratively to the reserved matches.
14. The RMS residual and χ^2 statistics are reported for the un-clipped detections on each exposure.
15. The input, output, and best-fit residual for every detection are written to an output FITS table for further offline analyses.

2.5. Performance

The run of WCSFIT producing the results in Section 4 was executed on a dual-CPU workstation with a total of 12 2.4 GHz cores. After reserving 30% of the matches, we fit 19 million detections in 311,000 distinct matches. There are 4948 map elements with a total of 26,645 free parameters. Each calculation of \mathbf{A} takes approximately one hour, and the linear solution takes one minute. Five iterations of minimization/clipping were required for convergence.

3. Input data

The astrometric solution is derived from multiple epochs of the star flat observations described above. Table 1 lists the dates and conditions of the star flat sequences during the first four years of DECam operations for which there were neither clouds nor instrument anomalies.³ functional CCDs at the start of Exposures are usually 30 s long, with 25–30 s dead time for readout and repointing, so the star flat sequence for 5 filters consumes about 2 hours of clock time. Figure 1 shows a typical star flat pointing sequence of 22 exposures. There are $\approx 10^5$ Gaia reference stars available in the area covered by the star flat exposures of a given field.

Each exposure is run through the standard DES data reduction pipeline, including linearization of images, crosstalk removal, correction for the “brighter-fatter effect” (Gruen et al. 2015), debiasing, and division by dome flats, and subtraction of sky and fringe signals. Sources are detected and measured using SExtractor (Bertin & Arnouts 1996). For the following analyses we filter the catalogs for sources with no SExtractor flags set, no defective, saturated, or cosmic-ray-flagged pixels within the isophote, with `MAGERR_AUTO` < 0.01, indicating signal-to-noise ratio $S/N \gtrsim 100$,

³Note that the number of functional CDDs on DECam dropped from 61 to 60 after one year of operation. Plots in this paper hence vary in the number of CCDs in use.

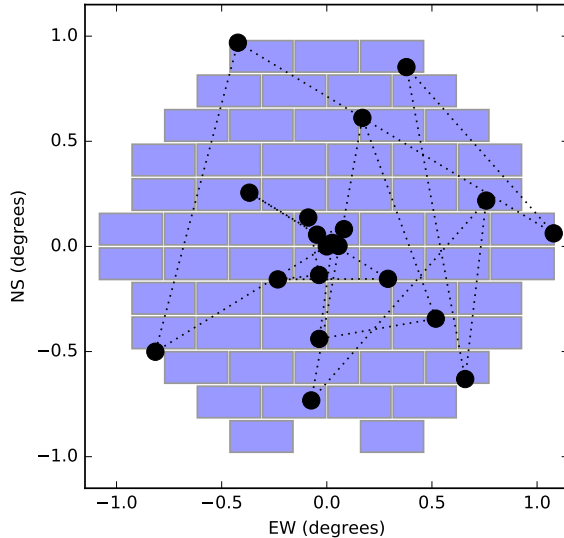


Fig. 1.— The dots show the pointing positions for a typical series of exposures in a single filter for a star flat sequence. These are overlain on an outline of the 61 functional DECam science CCDs as of December 2012. The dashed line connects the pointings in the order they are exposed.

and with $|\text{SPREAD_MODEL}| < 0.003$ to select only stellar sources. The flag cut removes objects that overlap detected neighbors.

The windowed centroids ($X_{\text{WIN_IMAGE}}, Y_{\text{WIN_IMAGE}}$) are used for centroid positions, \mathbf{x}^p , as they have been demonstrated to be robust to the details of the point-spread function (PSF) while approaching the accuracy of ideal PSF-fitting astrometry. Our focus on astrometric errors that correlate over space and/or time means we will not investigate the vagaries of centroid measurement, *e.g.* pixel-phase errors.

The density of useful stellar positions varies with field, filter, seeing, and sky conditions, but is usually 200-400 per CCD, or more than 10,000 per exposure and $> 10^6$ per star flat epoch.

4. The DECam astrometric model

Our goal is to produce an astrometric model that maps the \mathbf{x}^p of a source to ICRS sky coordinates, such that any *coherent* errors are at $\lesssim 1$ mas RMS. Coherence applies here to both time and space, meaning that the error should persist across more than one star and more than one exposure. Note that we are *not* attempting to model the following effects:

- Shifts in the centroids of individual detector pixels due to variation in lithography of the gate structures. There is not enough on-sky stellar data to calibrate this for the 500 megapixels in DECam. But astrometric errors due to pixel-to-pixel variations will behave as noise in

Table 1. Star flat observing sequences and DECam thermal events through Sep 2016

Epoch ^a	Field	D_{50} ^b	Airmass
20121120 ^c	0640–3400	2''09	1.04
20121223	0730–5000	1''04	1.06
<i>2012 Dec 30</i>		<i>Camera warmup</i>	
20130221	1327–4845	1''12	1.06
<i>2013 May 12</i>		<i>Camera warmup</i>	
<i>2013 July 22</i>		<i>Camera warmup</i>	
20130829	1900–5000	1''10	1.07
<i>2013 Oct 15</i>		<i>Camera warmup</i>	
20131115	0640–3400	1''41	1.09
<i>2013 Nov 30</i>		<i>CCD S30 fails</i>	
20140118	1327–4845	1''33	1.33
<i>2014 May 12</i>		<i>Camera warmup</i>	
20140807 ^d	1327–4845	1''43	1.32
20141105	0640–3400	1''28	1.01
<i>2014 Dec 1</i>		<i>Camera warmup</i>	
20150204	1327–4845	0''88	1.31
<i>2015 May 25</i>		<i>Focal plane temperature drop</i>	
<i>2015 June 25</i>		<i>Partial camera warmup</i>	
<i>2015 July 25</i>		<i>Camera warmup</i>	
<i>2015 Aug 9</i>		<i>Camera warmup</i>	
<i>2015 Aug 25</i>		<i>Camera warmup</i>	
20150926	2040–3500	1''19	1.01
<i>2015 Nov 26</i>		<i>Focal plane temperature drop</i>	
20160209	0730–5000	1''25	1.07
<i>2016 Feb 19</i>		<i>Camera warmup & corrector lens cleaning</i>	
20160223	1327–4845	1''10	1.24
20160816	1900–5000	1''08	1.06

^aThe local date at start of the night when the star flat exposures were taken or event occurred.

^bMedian half-light diameter of the point spread function for the i -band exposures in the sequence.

^c zY star flats were taken on the following night.

^d zY star flats were taken on 10 Nov.

individual stars’ positions, and will not correlate between stars. In well-designed use of DECam, a given star will be exposed on different parts of the array in each exposure, and hence this error will not correlate across time either. In any case, the RMS variation in DECam pixel sizes is estimated (from flat-field behavior) to be at a few parts per thousand, or < 1 mas. Stellar position errors will be even lower since they average over a PSF containing $O(10)$ pixels.

- Stochastic atmospheric distortions on $< 1^\circ$ scale. Such distortions are not coherent between exposures, but they are $\gg 1$ mas and dominate the astrometric error budget for high- S/N detections. The characteristics of these fluctuations are investigated in Section 6.
- Other sub-mas effects.

The DECam astrometric model was constructed through careful examination of the residual astrometric errors in the star flat data. The final choice of model is given in Table 2. Here we describe each element of the model in more detail, tracing backwards from the collected charge in the pixel well back to the top of the atmosphere.

4.1. Tree rings

In g , r , and i bands, photons generate holes near the DECam CCD surface and then have to drift the $250 \mu\text{m}$ thickness of the device before being collected in the pixels. As described in [Plazas *et al.* \(2014\)](#), any electric field components transverse to the surface will cause the charge carriers to drift sideways before collection and induce an apparent astrometric shift. The DECam CCDs are known to have two significant sources of such stray fields. The first are “tree rings,” which arise from fluctuations in the impurity density of the silicon boules from which the CCD wafers were cut. The zone refining of the boules results in approximate circular symmetry about the boule axis, and the wafers are cut perpendicular to this axis, so the astrometric distortions are realized as an irregularly oscillating pattern of rings. For some DECam devices, the ring centers are on the device, for others the centers are off their edges. Because the distortions also produce oscillations in the solid angle of sky received by each pixel, they are readily apparent in the flat-field images. The nearly-circularly-symmetric pattern in the flat fields implies that the astrometric distortions share this symmetry and are directed radially toward (or away from) the ring center. As described in [Plazas *et al.* \(2014\)](#), we locate the ring center for each CCD by visual inspection of the flat-field images, and then create templates of the expected astrometric distortion about this center from a high-pass-filtered, azimuthally averaged profile of the flat-field signal. Figure 2 plots the template derived for a representative device.

In WCSFIT, the tree ring signal is realized as a `Template` map, with both the variation and the displacement expected to be purely radial to the rings. We have a single free parameter for each device/filter combination, which is a multiplicative scaling of the distortion predicted by the template. We do not allow for any time variation of the tree ring signal, since the effect is literally built into the device. We do allow for a band dependence, however, since photons in the z and Y bands penetrate well into the device and are therefore expected to suffer less deflection before collection, on average. Figure 3 plots the best-fit template coefficients for all devices and filters. We

Table 2. Components of the DECam astrometric model

Description	Name	Type	Max. Size
Tree ring distortion	$\langle band \rangle / \langle device \rangle / rings$	Template (radial)	$\approx 0''.05$
Serial edge distortion	$\langle band \rangle / \langle device \rangle / lowedge$	Template (X)	$0''.03$
Serial edge distortion	$\langle band \rangle / \langle device \rangle / highedge$	Template (X)	$0''.03$
Optics	$\langle band \rangle / \langle device \rangle / poly$	Polynomial (order= 4)	$\gg 1''$
Lateral color ^a	$\langle band \rangle / \langle device \rangle / color$	Color \times Linear	$\approx 0''.04$
CCD shift	$\langle epoch \rangle / \langle device \rangle / ccdshift$	Linear	$\approx 0''.1$
Exposure	$\langle exposure \rangle$	Linear	$\gg 1''$
Differential chromatic refraction	$\langle exposure \rangle / dcr$	Color \times Constant	$\approx 0''.05$

^aThe lateral color correction is set to Identity transformation for izY bands.

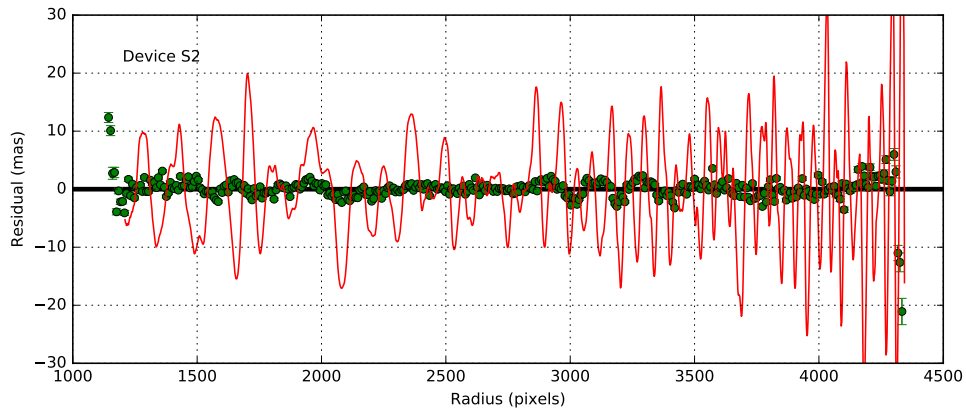


Fig. 2.— The red curve is the tree-ring astrometric displacement template derived from the r -band flat-field image of CCD S2. A spline-smoothed fit to the template is subtracted during its production to isolate the oscillatory portion that is due to the doping variations in the silicon boule. The green points and error bars plot the binned astrometric residuals for star-flat detections in gri bands on this detector. The azimuthally-averaged astrometric residual has been reduced to ≈ 1 mas RMS.

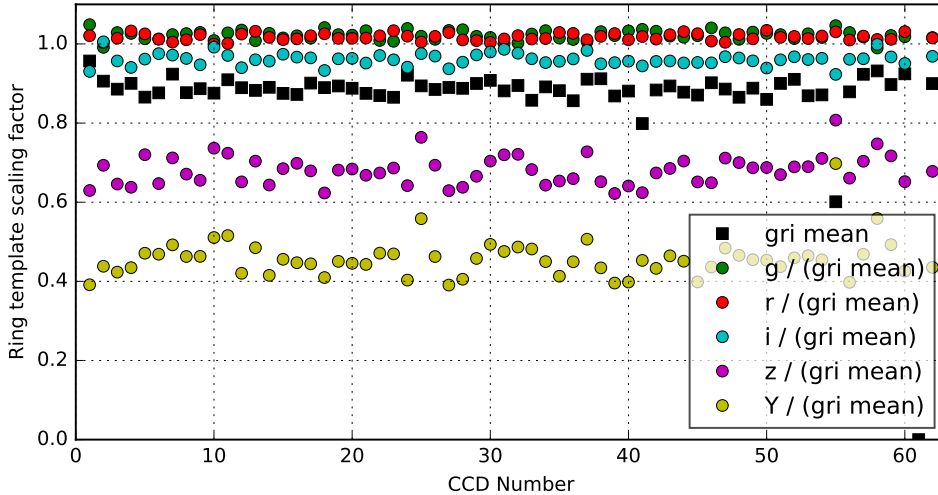


Fig. 3.— The best-fit coefficients for the tree-ring distortion templates are plotted vs filter for all of the functional CCDs. The coefficients are applied to the astrometric tree-ring pattern predicted from the r -band flat-field photometric rings. The black squares plot the mean, for each CCD, of the astrometric coefficients of the g , r , and i bands. The distortion is seen to be less than predicted by the flat-field templates, which is not understood. The other symbols show each filter’s distortion amplitude relative to the gri mean for that CCD. These values decrease for i , z and Y bands, as expected due their longer absorption length in silicon.

do not know, why the tree ring distortions are seen to be only 80–90% of the values predicted from the r -band flat-field images. But the scaling of these coefficients with filter band hews closely to the values calculated from the absorption-vs-wavelength characteristics of silicon. Figure 2 plots the azimuthally averaged residual position for all detections from the gri exposures of a representative device. The RMS of this residual is at our goal level of ≈ 1 mas.

4.2. Edges

The electric field in the CCD also develops a substantial transverse component near the device edges. The subsequent astrometric distortion and pixel-size variation is readily apparent in the flat-field images as a “glowing edge.” It is found that the flat-field (photometric) edge behavior is not a good predictor of the astrometric distortions, so we derive a template for edge behavior entirely from the stellar astrometry. We assume throughout that the edge distortion is directed in the x direction (parallel to the serial register on the short edge of the device) and is constant along y at each edge. We first fit the star flat data to a model with a `Piecewise` displacement term with a free node position every 8 pixels within 180 pixels of each edge.

Note that the 25 (15) pixels of the device nearest to the long (short) edges are completely masked from analysis because the distortion is too large. Thus we do not have useful stellar centroids closer than ≈ 30 pixels to the $x = 1, x = 2048$ boundaries. Any nodal values in these regions are unconstrained and ignored. There are also unusable nodal values near the locations of

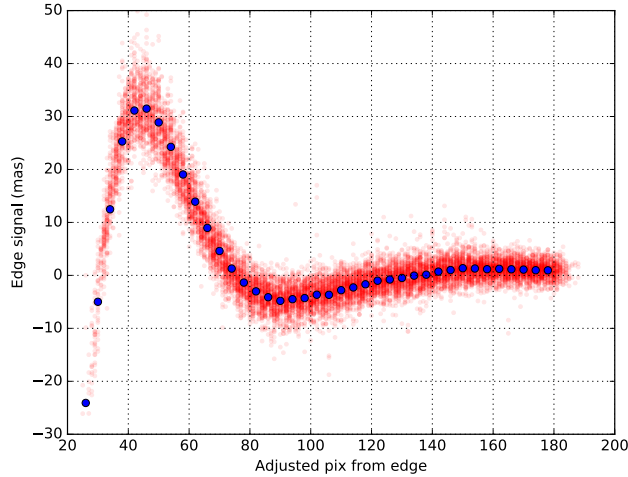


Fig. 4.— The master template for the x edge distortion is shown as the blue dots. Each red dot is a binned astrometric residual for a single device/edge combination in a fit *without* any modeling of the edge distortion, shifted horizontally by an amount judged to best align with the master template. The master template is derived from the median of all the red points, and is then used as a template for all x edge distortions. The model interpolates linearly between the blue dots.

any defective columns on a device.

Upon examination of the best-fit piecewise solutions at the x edges, we find that all edges of all CCDs in all filters are consistent with a common “master” edge template, once we allow for a multiplicative scaling and a shift as large as 12 pixels (0.18 mm). These shifts might come from the finite precision of the cutter tooling relative to the array during CCD dicing. The master edge template is shown in Figure 4. In the final astrometric fit, we allow each device/filter combination to have a `Template` pixel map at the high- and low- x edges. The templates are shifted versions of the master template, and the scaling is left as a parameter for WCSFIT to optimize.

Figures 5 plot the binned displacement residuals in all filters near all 4 edges of the CCD after the x -edge template is included in the WCSFIT model. The master template reduces RMS x residuals to well below 1 mas. Note that we have elected to make no correction at all for the glowing edge effect on the short (y) edges, because the displacement is already < 3 mas before correction. Since it affects only a small fraction of the focal plane, the RMS error is $\ll 1$ mas.

The best-fit coefficients to the master template are found to be in the range 0.8–1.2 in the gri bands, with lower values in z and Y as expected again from the deeper photon conversion. We take the edge coefficients to be independent of time, as one would expect for such detector-physics effects.

4.3. Optics polynomials

The vast majority of the nonlinearity in the $\mathbf{x}^p \rightarrow \mathbf{x}^w$ map is produced by the classical distortion of the optical system. A time-independent polynomial map for each filter/device combination, with

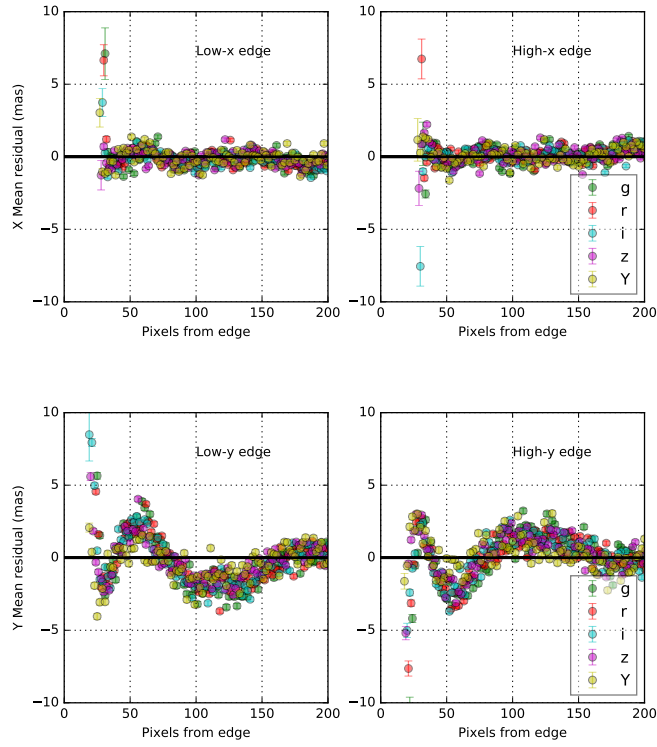


Fig. 5.— Each panel shows the mean residual distortion vs distance from the CCD edge, after our final WCSFIT model which includes a multiple of the master template for the x edges. In each case we are averaging the displacement component perpendicular to the CCD edge. The master template is seen to reduce RMS x edge residuals to $\ll 1$ mas. We have not implemented a correction for the y edges because the signal is < 3 mas in all cases and affects only a few percent of the focal plane. These plots average over all CCDs in the northern half of the array; the southern CCDs are installed with 180° rotation and would swap the high and low sides. Plots for individual CCDs are consistent with noisier versions of the mean behavior.

terms $x^m y^n$ up to order $m + n \leq 4$, is used. While the camera optics have radial distortion at fifth (and higher) order, a fourth-order-per-CCD solution is found sufficient to capture the optical distortion, and the placement of the CCDs in the focal plane. These polynomials carry 30 free parameters per CCD per filter, roughly 9000 for the whole array. It is in this map that we change units from pixels (on the array) to degrees (in the gnomonic projection about the telescope axis).

4.4. CCD shifts

The DECam astrometric map is observed to change over time by $O(100)$ mas. We posit that these changes are dominated by small translations and rotations of the devices with respect to their mounting plate, or other mechanical drifts. We allow WCSFIT to model this by adding a linear (affine) distortion, with 6 free parameters, to each CCD, for every star flat epoch except the first one. The CCD shifts are taken to be identical in all filters. The results of these fits are examined in Section 7.

4.5. Lateral color

Any axisymmetric refractive optical system is expected to have color-dependent radial distortion, leading to color terms described by odd-order polynomials in radius. We check this assumption by including in our initial fits a more general color term: a time-independent linear function of coordinates on each CCD. The displacement is assumed to be proportional to

$$c \equiv (g - i) - (g - i)_{\text{ref}}, \quad (20)$$

where the reference color is chosen to be 0.44, the color in the natural DECam ($g - i$) system of the F8IV star C26202 from the Hubble Space Telescope CalSpec system.⁴ We restrict the fit to stars with $-0.2 \leq (g - i) \leq 1.8$, to avoid M stars for which the expected shifts may no longer be linear in c , and assume that the color term is time-independent for a given filter.

Figure 6 plots the best-fit static color solution in the g and r bands, which show the radial patterns (at mas accuracy) and approximate amplitude expected from the optical solution (S. Kent, private communication). The solutions for i , z , and Y bands are, as expected, undetectably small as the chromatic terms of the corrector lenses are weaker, and we disable their color terms for the final WCSFIT run. For the g and r bands, we continue by re-fitting to a more restrictive function, namely a `Color` pixelmap wrapping a radial `Piecewise` displacement. A fifth-order function of field radius is found to fit the resultant piecewise function with 2 mas/mag RMS scatter (Figure 6). We used the fitted polynomials (implemented as radial `Template` pixel maps) for our final model, with no free parameters.

⁴<http://www.stsci.edu/hst/observatory/crds/calspec.html>

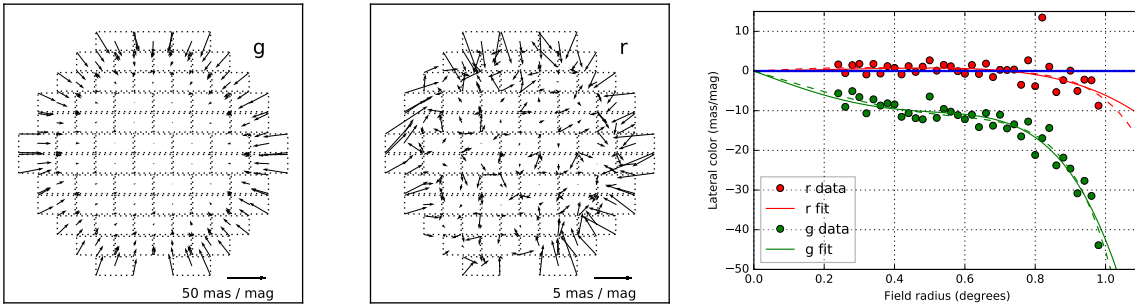


Fig. 6.— The best-fit solutions for static color-dependent distortion are plotted for g (left) and r (center) bands. Note the very different scales for each. The dashed rectangles are the outlines of the 61 DECam CCDs that have been functional for at least part of this analysis. The arrows plot the shift per magnitude of $g - i$ color at the four corners of each CCD, using the best-fit model of linear dependence across each device. As expected from the optical design, the pattern is radial, with barely detectable amplitude in r band and no detectable i , z , or Y band lateral color (not shown). At right are the results of fitting the g and r data to a purely radial piecewise function of radius (circles). We adopt as our final lateral color model the fifth-order polynomial fits to these models (solid lines), as a seventh-order fit (dashed lines) offers no significant improvement.

4.6. Exposure solution

Aside from the freedom to determine the pointing of the optic axis on each exposure, we will clearly require the model to admit exposure-to-exposure freedom to rotate, shear, and magnify the image across the FOV, because these effects will be present (at many mas) due to misalignment of the telescope equatorial mount, temperature-induced variations in focal length, atmospheric refraction, and stellar aberration from Earth’s motion. An active optics system (Roodman et al. 2014) controls the position of the camera and corrector with respect to the primary mirror; variations in this position could also induce small time-dependent changes to the optical distortion. We proceed with this linear freedom per exposure in our analyses. As noted earlier, atmospheric refraction should generate quadratic terms at $O(10)$ mas; we will subsume these into our investigation of stochastic atmospheric distortions in Section 6.

4.7. Differential chromatic refraction

The color dependence of atmospheric refraction in the context of wide-field cosmological surveys is studied by Plazas & Bernstein (2012) and Meyers & Burchat (2015), who conclude that in some bands it will be present at $O(10)$ mas and significant for weak gravitational lensing analyses. The atmospheric refraction is very large ($1' \times \tan z$ at zenith angle z) compared to our desired accuracy so the chromatic effect is significant. For a given site it is expected to behave as

$$\Delta \mathbf{x}^w = K_b c \tan z \hat{\mathbf{p}} \quad (21)$$

where c is the object color (again $g - i$), $\hat{\mathbf{p}}$ is the unit sky vector toward the zenith (the parallactic angle), and K_b is a constant derivable for each band b from the instrumental bandpass and

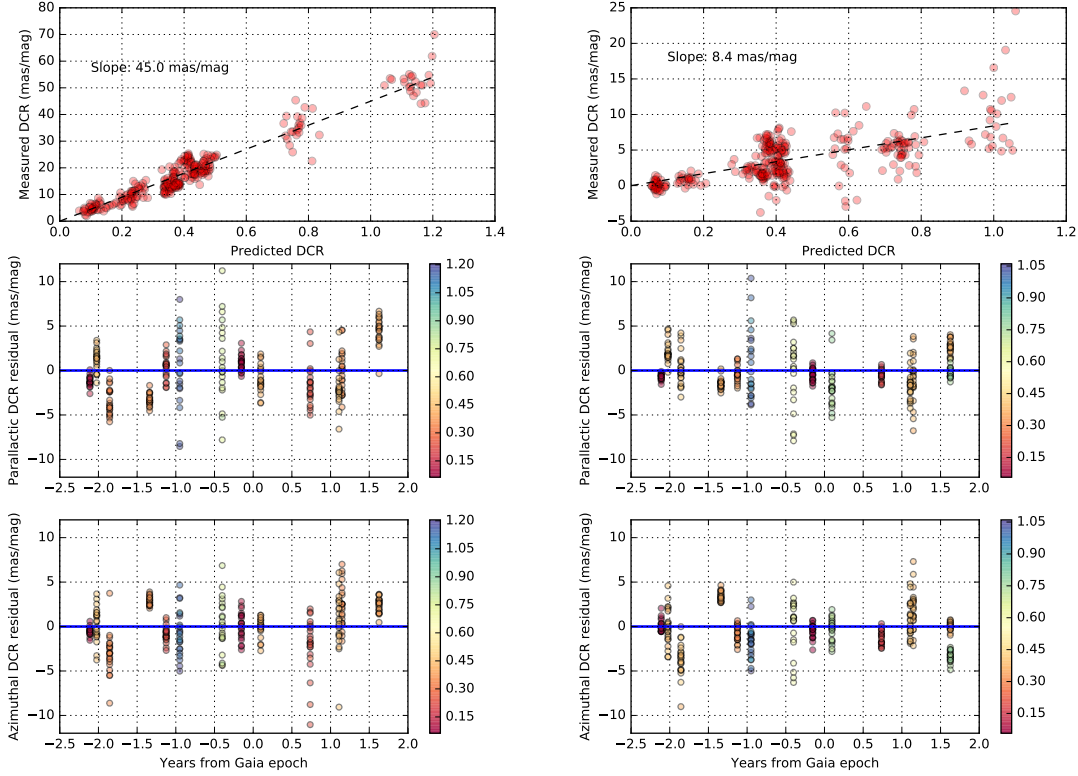


Fig. 7.— The derived differential chromatic refraction (DCR) for the g and r star flat exposures (left and right columns, respectively) are compared in the top row to the predicted scaling with $\tan z$. The top row plots the measured DCR component along the parallactic (zenithal) direction, with the dashed line showing the prediction Equation (21) with the best-fit value of K_b for each band b . The middle row plots the residuals to Equation (21) vs the date of the exposure, with the points color-coded according the value of $\tan z$. The bottom row plots the azimuthal component of the measured DCR, which is expected to be zero. The model works well, with 2–3 mas/mag RMS residuals, and no remnant trends with time or airmass.

atmospheric index of refraction.

We test this model by allowing each exposure to have its own constant differential chromatic refraction (DCR) term $\Delta \mathbf{x}^w$ when fitting to the star flat detections. Figure 7 shows these results for g and r bands, along with the model (21) with the best-fit value of K_b . The standard atmospheric model is seen to describe the measured $c \Delta \mathbf{x}^w$ well, with RMS residuals of 2–3 mas/mag. Table 3 gives the DCR amplitudes K_b derived from the star flat data (supplemented with the supernova field data described in Section 7 for the i and z bands). The K_b are in good agreement with the predictions of Plazas & Bernstein (2012), and for future use it should suffice to simply fix the DCR term to Equation (21) instead of allowing freedom to each exposure.

5. Unmodelled distortions

The first panel of Figure 8 plots the errors $\Delta\mathbf{x}$ in the stellar positions of a randomly selected single exposure on a randomly selected CCD, relative to the mean positions determined for the same stars from the entire stack of star-flat exposures. The residuals after application of our final astrometric model are dominated by a coherent pattern with RMS $|\Delta\mathbf{x}| \approx 15$ mas. This pattern is found to differ from exposure to exposure and is plausibly attributed to refraction by atmospheric turbulence. Before investigating these stochastic distortions in Section 6, we ask here whether there are any distortion patterns that recur from exposure to exposure. To find them we will need to average down the stochastic atmospheric signal by stacking and binning the residuals from many exposures.

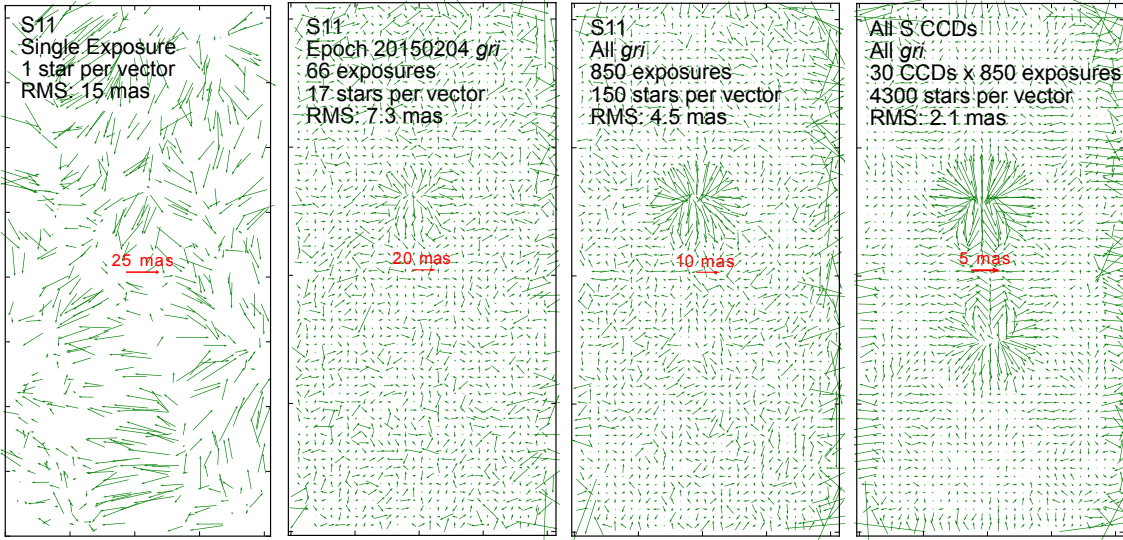


Fig. 8.— Astrometric errors as a function of CCD position are shown at left for all detections on a randomly selected detector (S11) in a single exposure. The pattern is dominated by atmospheric turbulence. Succeeding panels average larger sets of data in bins of CCD position order to reduce the atmospheric signal and reveal persistent errors in the astrometric model. Note the change of scale in each panel.

The middle panels of Figure 8 show the result of averaging the residuals from all of the $g, r,$

Table 3. Differential Chromatic Refraction for DECam

Band	K_b (mas/mag)
g	45.0
r	8.4
i	3.2
z	1.4
Y	1.1

and *i* band exposures from a single star flat epoch, and then from all epochs. The amplitude of the residual pattern drops steadily with number of exposures included, although not as quickly as the square root of the number of exposures, as would be expected if all remaining errors were uncorrelated between exposures. The all-*gri* residuals for this CCD exhibit clear coherence of several kinds:

- A radial pattern just above center contains distortions with amplitude of up to 30 mas. This roughly coincides with the edge the electrical connector that is soldered and glued to the CCD, and protrudes through a hole in the CCD mounting board. The right-hand panel of Figure 8 averages over all 30 functional DECam science CCDs mounted in the same orientation, showing that this pattern is recurrent and exists at both ends of the connector mount, and is likely a product of stresses induced in the CCD lattice the connector or the hole in the mounting board.
- There are excess residuals along the long edges of the device, suggesting that the edge distortion is not uniform along the edge of the device. The rightmost panel confirms that this is true in a systemic fashion for the devices.
- The right-most panel shows the largest residuals in the corners of devices, plus two patches at the midpoints of the long edges. These six locations are known as “tape bumps” since they are underlain by thin spacers that define the thickness of the glue layer between the CCD and its carrier. These regions, each 100–200 pixels on a side, exhibit structure in the flat fields that is indicative of stray transverse electric fields induced by lattice stresses. There are clear astrometric disturbances associated with these fields as well. Because these are difficult to model and cover only a small fraction of the focal plan, we do not attempt to remove them: detections occurring on the tape bumps are flagged as having less reliable astrometry, and in fact have been omitted from the characterization and modeling performed in this paper.

The DECam flat fields show evidence for modulations of the pixel size with period $\Delta x = 27.33$ pixels, a behavior seen in many CCDs due to the step-and-repeat accuracy of the mask generator (Anderson & King 1999). A corresponding periodicity is detectable in the astrometric deviations, but with peak-to-peak amplitude < 1 mas, as is predicted from the amplitude of the flat-field fluctuations. We ignore this effect for DECam.

A final question we address about the residuals to the model is whether the linear-per-ccd `ccdshift` terms are sufficient to describe the change of the astrometric solution between epochs. Figure 9 shows a test of this, whereby we plot the mean residual astrometric errors for an entire epoch’s *gri* detections, averaged by position on the array. The residuals are consistent with the expectations of averaging 66 realizations of the stochastic atmospheric pattern. In particular there are no statistically significant discontinuities across CCD boundaries.

We conclude that our astrometric model captures the recurrent instrumental distortion pattern to an accuracy of 2–4 mas RMS. The only residual distortions that have detectable coherence between the 64-pixel (16”) bins of Figure 8 are those associated with stresses from the CCD mounting, and with inhomogeneities in the transverse electric fields generated at the CCD edges.

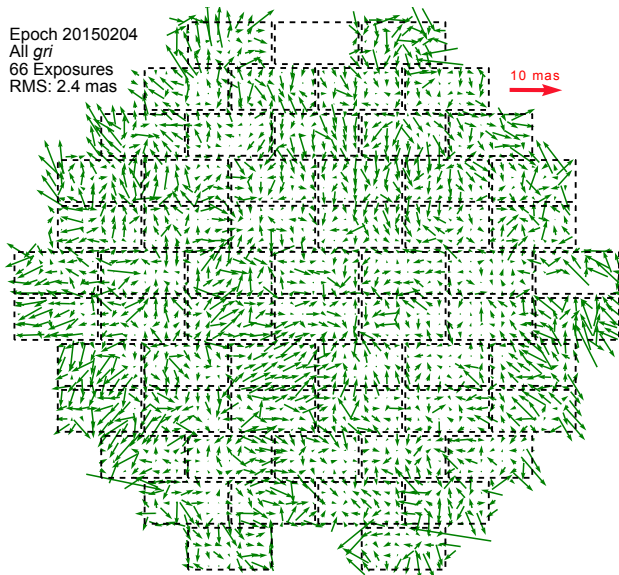


Fig. 9.— The mean astrometric error of all detections in the g , r , and i bands during star flat epoch 20150204 is plotted vs array position. No discontinuities at device boundaries are detectable (dashed boxes), and the signal is consistent with our model in which epoch-to-epoch changes are fully captured by linear adjustments to each CCD, plus the stochastic atmospheric signal. The DECam FOV is 2° in diameter, and the distortion field is magnified by $\approx 50,000$ to conform to the red scale bar.

6. Stochastic errors

After application of the astrometric model, the dominant form of astrometric error is a field that varies from exposure to exposure and has a coherence length of $5\text{--}10'$. Figure 10 plots the residual vector field for a representative exposure.

6.1. Atmospheric turbulence

Multiple lines of evidence support the hypothesis that these distortions arise from refraction by atmospheric turbulence:

- The patterns are uncorrelated between exposures, and thus change on time scales of 1 minute or less. The only physical conditions that should change this quickly are the atmosphere and the settings of the hexapod that fixes the alignment of the camera to the primary.
- The distortion pattern appears to be curl-free. The lower panel of Figure 10 suggests that the curl arises from white noise, *i.e.* errors in stellar positions due to shot noise. This is shown more rigorously in Figure 11, in which the 2-point correlation function of astrometric errors is split into E- and B-mode components (curl- and divergence-free, respectively), as explained in Appendix A. The latter is seen to be consistent with zero. Curl-free distortion patterns are expected in the ray-optic limit, where the astrometric displacement of each photon is the

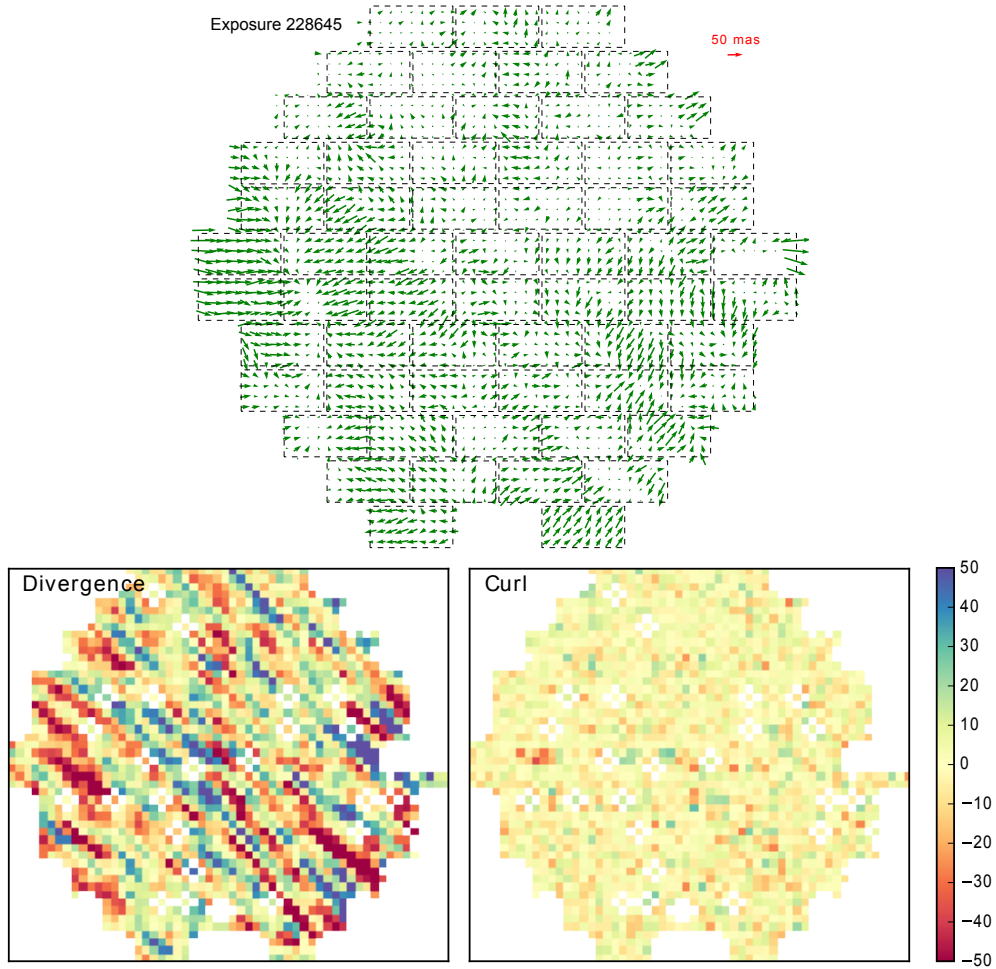


Fig. 10.— At top are the astrometric residuals of detections in a representative exposure (228645, z band), averaged in bins of focal-plane position. Below are the divergence and curl of this vector field, plotted on a common scale. The continuity of the vector field across chip boundaries, the curl-free nature of the field, and the streaky pattern of divergence strongly support the hypothesis that these distortions arise from atmospheric turbulence.

gradient of the integral of the scalar index of refraction (time delay) along the line of sight to the star.

- The distortion pattern is clearly anisotropic, with a long correlation length in one direction. The preferred direction is roughly, but not exactly, consistent between exposures, as is expected from having the atmospheric turbulence pattern blowing across the field of view during the exposure. The streaky patterns are very similar to the maps of PSF ellipticity in short exposures with the CFHT Megacam presented by [Heymans et al. \(2012\)](#), which they also attribute to wind.
- The power spectrum of the distortion in the cross-wind direction is roughly consistent with

that expected of Kolmogorov turbulence.

- The amplitude and correlation length of the distortion are roughly consistent with numerical simulations of Kolmogorov turbulence (J. Peterson, private communication). The simulations suggest that the astrometric perturbations are strongly dependent on the outer scale of the turbulence.

If the stochastic distortions do indeed arise from atmospheric turbulence, we expect their amplitude to decrease with the square root of exposure time as we average over phase screens. We cannot verify this with our data since nearly all star flat exposures were taken with 30 s exposures, save the first three epochs which used 50 s. While these early epochs do show the lowest stochastic distortion (see Figure 12), there is substantial variation from epoch to epoch so we cannot draw any quantitative conclusions.

6.2. Behavior of the stochastic component

For a more quantitative picture of the stochastic/atmospheric distortion field, we produce its 2-point correlation function

$$\xi_+(r) \equiv \langle \Delta \mathbf{x}_i \cdot \Delta \mathbf{x}_j \rangle_{|\mathbf{x}_i - \mathbf{x}_j| = r}, \quad (22)$$

where \mathbf{x}_i is the sky position of detection i , $\Delta \mathbf{x}_i$ is the measurement error on this position, and the average is taken over all pairs of detections $i \neq j$ in the *same exposure* separated by distance r (in practice the “true” position is taken as the average of our many measured positions). Appendix A explains how ξ can be split into two components ξ_E and ξ_B which arise from the curl- and divergence-free parts of the vector field, respectively. These are plotted in Figure 11, where it is clear that ξ_B is insignificant in comparison to ξ_E , as expected for atmospheric refraction. In this case, and if we consider the turbulence to be a Gaussian random field, then $\xi_E = \xi_+$ fully characterizes the field.⁵

Before calculating ξ , we subtract from the $\Delta \mathbf{x}_i$ the best-fit cubic polynomial function of field coordinates. As discussed earlier, we expect significant linear and quadratic-dependence distortions from normal (homogeneous) atmospheric refraction; turbulent refraction should also have a substantial large-scale component, and indeed we observe $\approx 25\%$ of the distortion variance to come from this polynomial signal. Since the low-order component is easily determined in practice by fitting to the Gaia catalog, we remove it from our analysis, leaving small-scale distortions. Note that the virtue of using $\xi(r)$ is that it is unaffected by the shot-noise measurement errors of the stellar positions (for $r > 0$) and therefore is a pure measure of the astrometric map.

We characterize the astrometric correlation function by two quantities, ξ_0 and R_{corr} . The former is essentially the small-scale (largest) value of ξ_+ , defined as

$$\xi_0 \equiv \frac{\int_0^\infty r dr W(r) \xi_+(r)}{\int_0^\infty r dr W(r)} \quad (23)$$

$$W(r) \equiv e^{-r^2/2\sigma^2}, \quad \sigma = 1'. \quad (24)$$

⁵A complete description would require inclusion of directional dependence of ξ since the field is anisotropic.

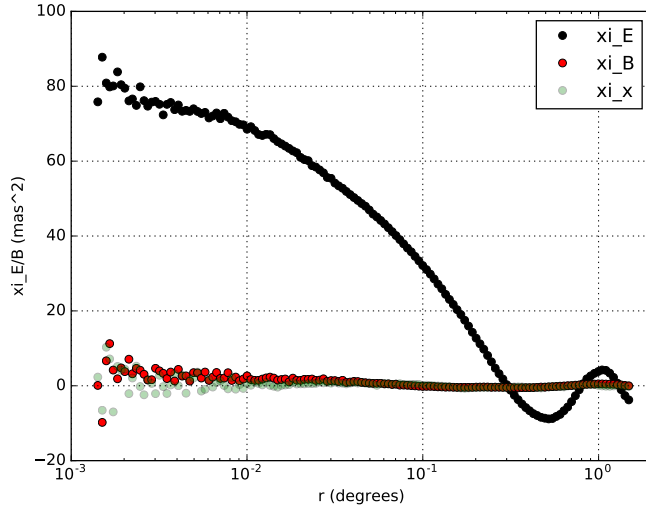


Fig. 11.— Two-point correlation function $\xi(r)$ of the astrometric errors, averaged over 20 z -band exposures in the 20121120 epoch, which exhibits the weakest stochastic distortion signal. The signal is split into ξ_E (the ξ of the curl-free portion of the vector field), ξ_B (divergence-free), and the cross-correlation ξ_x between these two. As expected for any parity-invariant process, ξ_x is consistent with zero. Atmospheric refraction should have $\xi_B = 0$, consistent with the observations. The oscillations in ξ_E at r above $\frac{1}{4}$ of the field diameter are to be expected, since we have subtracted the best-fit cubic polynomial from the residual pattern.

The second quantity R_{corr} is defined as the radius at which $\xi_+(R_{\text{corr}}) = 0.5\xi_0$, *i.e.* the smoothing scale that would cut the astrometric variance in half.

Figure 12 plots the values of ξ_0 and R_{corr} for all the star flat exposures under analysis, along with the half-light diameter D_{50} of the PSF in each exposure. It is clear that there are nights when a degradation of seeing is accompanied by an increase in astrometric distortion (*e.g.* 20140118, 20150926), as one might expect if both are proportional to the amplitude of a strictly Kolmogorov turbulence spectrum. However there are also cases of anti-correlation, and the mean seeing of a night is a very weak predictor of astrometric accuracy. In particular, the epoch 20140807 is astrometrically awful, exhibiting 30–50 mas RMS atmospheric contribution whereas most other epochs are 10–20 mas RMS. Yet the seeing on that night was not as poor. Clearly there are other variables besides Kolmogorov amplitude, such as wind speed or outer scale, that determine the astrometric quality of the night.

The correlation angle is in the range $4' < R_{\text{corr}} < 10'$ at all epochs, with no apparent relation to the seeing. This suggests that interpolation between stars in Gaia catalog, with source density of ≈ 1 star per arcmin² at high latitude, could significantly reduce the stochastic atmospheric errors. We investigate this in Section 8.

The DECam measures of stochastic atmospheric astrometric fluctuations are in rough agreement with previous characterizations by Han & Gatewood (1995), Zacharias (1996), and Bouy et al. (2013) (and references therein), in terms of typical amplitude at good sites, and substantial night-to-night variation that is at best tenuously tied to the seeing FWHM.

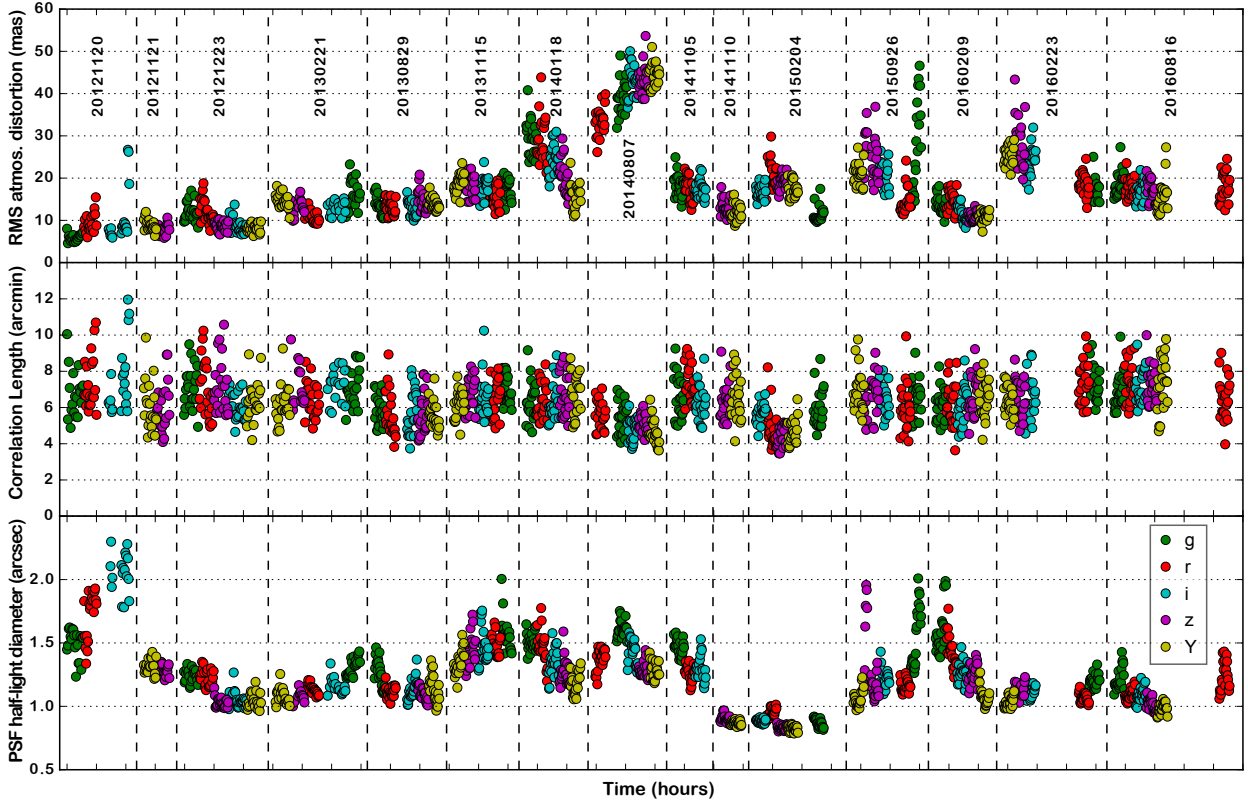


Fig. 12.— The RMS stochastic astrometric distortion $\sqrt{\xi_0}$ (top), the correlation length R_{corr} of the distortion, and the half-light diameter D_{50} of the PSF are plotted vs time for all star-flat exposures. Each horizontal tick marks one hour, and the vertical lines represent the days to months between sets of star flat observations. Epochs are labelled across the top. The amplitude of astrometric distortion is only partially correlated with the seeing.

7. Solution stability

Is the DECam astrometric solution stable over weeks, days, or years? We already know that there is short-term (seconds) variability due to atmospheric turbulence, at a typical level of 10–20 mas RMS in a 30 s exposure and 5–10' correlation length. But this should average to zero with longer exposures. We have verified in Section 5 that the astrometric errors within a given star flat epoch (*i.e.* a few hours' clock time) are consistent with a single solution, up to the accuracy allowed by the stochastic atmospheric distortions, as long as we allow for expected exposure-to-exposure variations at low order across the focal plane. We are interested in the duration over which a single astrometric solution can otherwise be considered to maintain few-mas accuracy.

Our fit to all of the star flat data allowed for variations between star flat epochs in the form of a free linear transformation for each device. Figure 13 depicts the “CCD shift” patterns found to best fit 5 of the epochs. In these plots, and in all analysis, we removed from the CCD shift coefficients any components consistent with an overall cubic polynomial distortion of the focal plane, since we know that the solution will have time variability of this nature which must be resolved on an

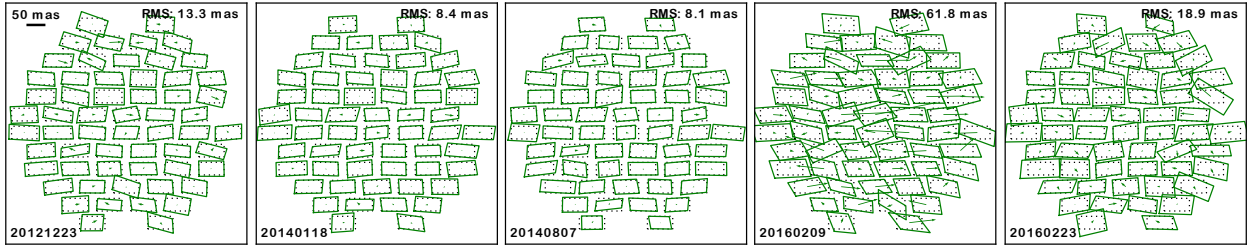


Fig. 13.— The CCD shifts derived for a subset of the star flat epochs are shown, after removal of any exposure-wide cubic polynomial distortions. In this and subsequent figures, the motion of the center of each CCD is indicated by the arrow, with scale shown in the upper left. The green rhombi show the distortion of each CCDs shape, exaggerated such that the shift with respect to the (undistorted) black outlines depicts the distortion of the device at a scale corresponding to the bar. The epoch-to-epoch shifts can be large relative to the typical stochastic atmospheric distortions. Note that the last two epochs plotted are only 14 days apart but differ by > 100 mas in places.

exposure-by-exposure basis, *e.g.* by using Gaia reference stars. The Figure makes it clear that there are epoch-to-epoch changes that would dominate the stochastic errors even in a single 30 s exposure. The relative motions of CCDs can be surprisingly large, *e.g.* over 100 mas, or $> 6 \mu\text{m}$ in the focal plane, over a time period of just 14 days, in the case of the last two epochs plotted.

The star flat sequences were taken too infrequently to resolve the temporal behavior of the CCD shifts. Fortunately the *Dark Energy Survey* observing program includes repeated visits to 10 fields in a search for high-redshift supernovae. Each field is imaged roughly once per week during the 6-month DES observing season. We examine here the stellar detections in ≈ 1500 exposures taken of the SNC3 field in the 4 years following camera commissioning. Visits to this field usually comprise 3×200 s exposures in g band, 3×400 s in r , 5×360 s in i , and 11×330 s in z . After matching all of the stellar detections in these images, we run WCSFIT on the 1123 i and z band exposures from 112 distinct nights during which the photometric solutions indicate absence of clouds and the seeing D_{50} is predominantly $< 1''.6$. This WCSFIT adopts the astrometric solution derived from the star flats, holding all parameters fixed except:

- the linear solution for each exposure,
- the differential chromatic refraction constant for each exposure, and
- the linear CCD shifts, one per CCD per epoch (night) of observations.

From this solution we extract the CCD shifts for each SNC3 epoch, combining them with the CCD shifts for the star flat data, and projecting out a FOV-wide cubic polynomial fit to each epoch. We analyze only the 59 CCDs that are fully functional over the 4 years.

The first row of Figure 14 plots the difference between each epoch’s CCD shifts and the preceding epoch’s solution. We quantify this difference by giving the RMS displacement between the solutions, averaged over the active regions of the array. We see immediately that the largest changes occur for the first epoch to follow a warming or cooling event for the camera. DECam is cycled to room temperature for various maintenance purposes, or when electrical power is lost for

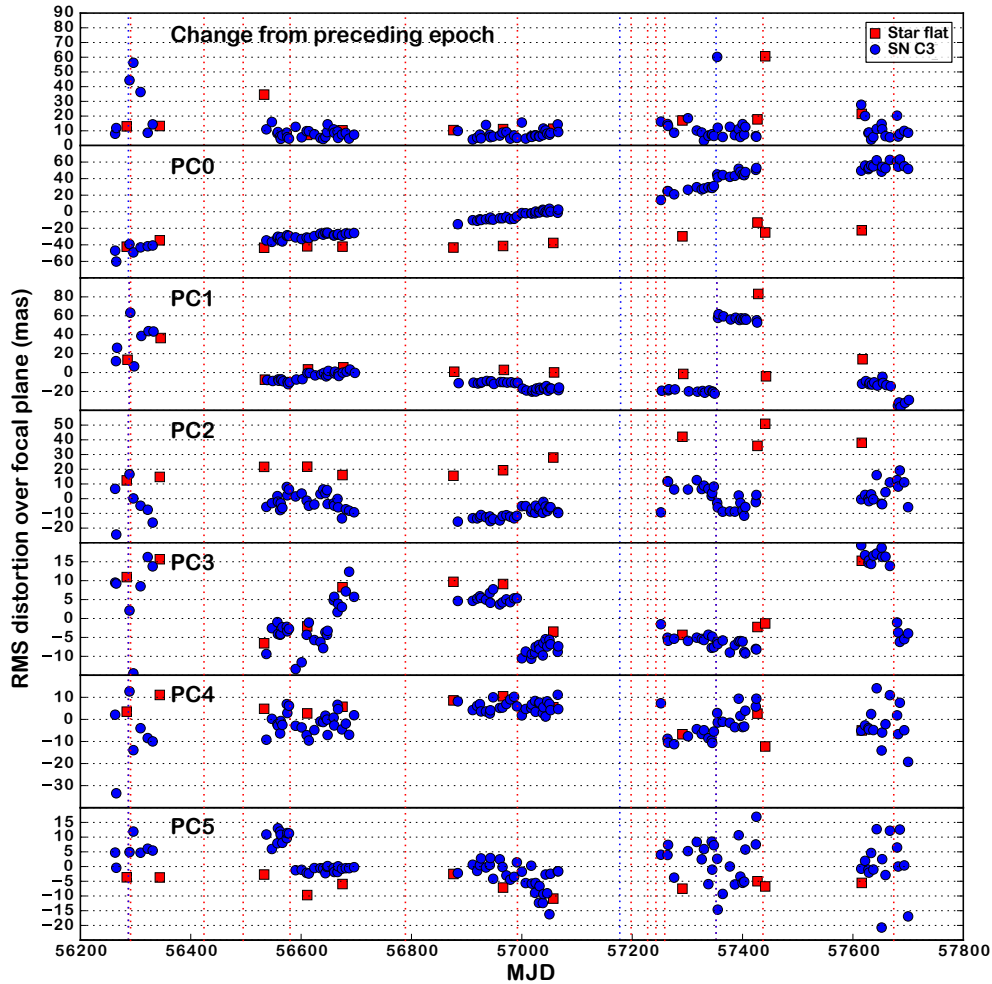


Fig. 14.— The top row shows the RMS change across the FOV in the CCD shift solution between each epoch and its predecessor, plotted against date of observation. The largest changes occur for the epochs following a warming of the camera to ambient temperature (marked by red vertical dashed lines) or a cooling of the focal plane to -120 C (blue vertical lines). Star flat epochs are distinguished from supernova C3 observations as per the legend. Further rows show the RMS contributions to each epoch’s CCD shifts of the first six principal components of variation. See the text for further narrative.

long periods. On three occasions the focal plane temperature dropped from the normal -100 C to -120 C when power to its heaters was lost for several hours. We will refer to these as “camera events” and the periods between them as “camera intervals.”

We perform a principal components analysis of the 354-element feature vector specifying each exposure’s CCD shifts, in hopes of revealing the temporal structure of the largest contributors to astrometric variation. We should be aware, however, that two spurious signals will be present in these data:

1. The SNC3 exposures are taken with minimal dithering, and have only ≈ 20 high- S/N stars

per CCD, many fewer than the star flat data. This means that the CCD shift fits will be pulled by the proper motions of the stars within each device. We should therefore expect to see one or more principal components (PCs) containing a signature that is linear in time for the SNC3 exposures and absent from the star flat exposures. Parallax motion of the SNC3 stars should be a small perturbation to this.

2. The SNC3 CCD shifts have a different reference epoch than the star flat solution’s. Therefore we should see a static difference between these two in at least PC.

Figure 14 presents the coefficients of the six most significant PCs, plotted against date of the epoch solution. These are again plotted in units of the RMS displacement they represent on the focal plane. We immediately identify PC0, the largest contributor, as the expected signature of proper motion in the SNC3 stars (although it is also possible that a smaller, linear-with-time focal plane drift is also in this PC). We also suspect that PC2 contains the second expected spurious signal, the distinct reference epochs for the SNC3 and star flat solutions.

Most striking is that the other PCs appear to be dominated by changes that occur at camera events. The largest, PC1, began on Thanksgiving Day 2015, and its associated distortion persisted at normal operating temperatures until the camera was warmed on 19–23 Feb 2016. Note that this warmup occurs between the last two star flat epochs plotted in Figure 13. Figure 15 plots the change in focal plane mapping that occurred during this cooldown. Some of the CCDs appear to have moved by up to 100–150 mas, or 6–10 μm . CCDs also show significant rotations, contributing ≈ 20 mas RMS displacement. Scale changes or shears of the CCDs are much smaller ($\lesssim 3$ mas RMS), as expected if the cooldown distorted the mounting structure.

Concluding that *the bulk of the change in astrometric maps occurs during camera events*, we adopt a scheme for astrometric calibration of DES data whereby **each exposure is assumed to have the same instrumental astrometric map as the nearest-in-time star flat epoch that lies within the same camera interval.**

We test this DES astrometric procedure by re-running WCSFIT on the SNC3 *iz*-band exposures using a model with the CCD shifts assigned per the local star flat data, and allowing each exposure a free cubic polynomial distortion across the focal plane.⁶ We fit a linear function of time to each SNC3 star’s measured positions and subtract these to yield measurement errors free of proper motion.

Figure 16 illustrates the quality of the resulting fits. In the top row we plot the RMS deviation of all stellar residuals from a given night relative to the mean *within* the night. This is a measure of astrometric map components that vary on time scales of hours or less, which we expect to be dominated by atmospheric effects. At 5–7 mas RMS per component, these are roughly consistent with the values seen in Figure 12 after considering the $\sqrt{330/30} \approx 3.3\times$ reduction in atmospheric noise expected from the longer exposure times in the SN field. It is also possible that some of this RMS is due to unmodelled instrumental effects that vary across the 10–20'' dithers of the supernova exposures, *e.g.* the pixel-to-pixel fluctuations in CCD gate lithography.

⁶A small number of SNC3 epochs do not have any star flats taken in the same camera interval; these are not included in Figure 16.

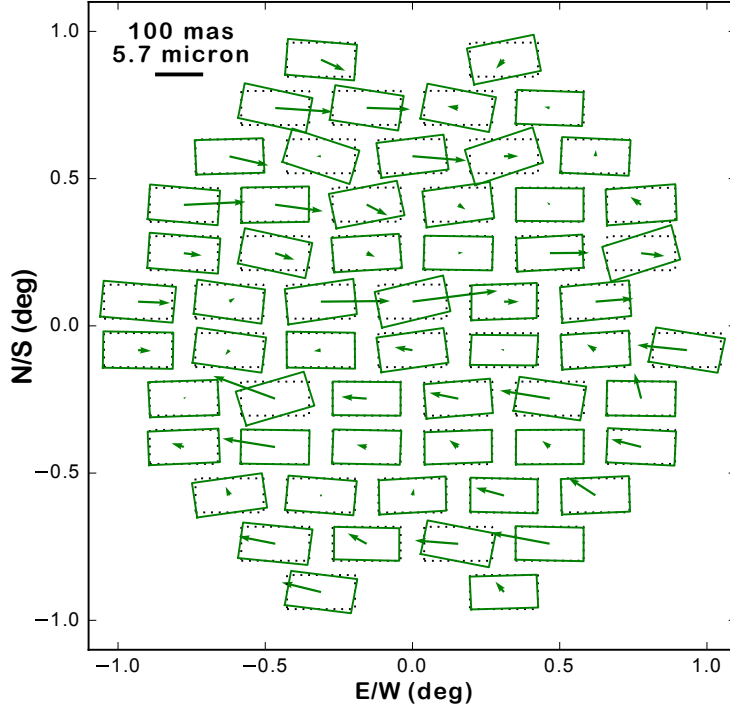


Fig. 15.— The CCD shifts that occurred during the focal plane cooling of 26 Nov 2015, *i.e.* PC1. Devices translate as much as 200 mas, nearly a full pixel, and undergo substantial rotation. Shear and magnification are small (< 3 mas RMS), as expected if the shifts are due to displacements of the CCD carriers.

The lower panel of Figure 16 plots the RMS deviation of each night’s stellar exposures after we *average the night’s measurements of each star and subtract the noise expected from the intra-night variations*. This yields an estimate of the RMS astrometric error that is coherent through a night, such as might be attributable to unmodelled shifts in the CCD positions or changes in optical alignment. Such errors are seen to be in the 2–4 mas range on most nights. The errors appear larger in the E-W direction than the N-S direction, particularly during early Y1 observations when the E-W errors reach 6 mas RMS, perhaps indicating lower quality in the star flat solution derived for the corresponding camera interval.

We note, finally, that the cubic polynomials we fit to each exposure are often much larger in amplitude than could be ascribed to atmospheric effects. This suggests that changes in optical alignment over time are significant at ~ 100 mas level.

8. Interpolation schemes

Given an astrometric reference catalog with errors at mas scale and > 1 star in each 5–10’ coherence patch, one could measure some fraction of the atmospheric (or other) astrometric errors and add them to the solution, *i.e.* interpolate the map between reference stars. The Gaia catalog will provide such a reference catalog. The Gaia DR1 secondary catalog ([Gaia Collaboration 2016](#))

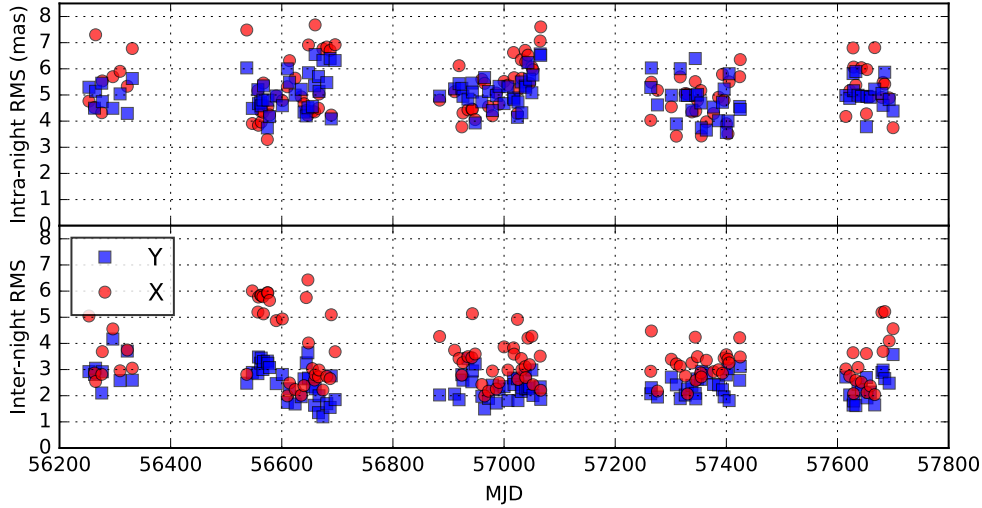


Fig. 16.— The RMS errors of each night’s SNC3 stellar positions are plotted after each exposure has been modelled with CCD shifts taken from the temporally nearest star-flat image, and a free cubic polynomial distortion across the focal plane. A linear proper motion has been fit to and removed from each star’s measurements. The upper panel plots the RMS residual of single-exposure positions relative to the mean position of the star on that night, *i.e.* it gives the amplitude of stochastic atmospheric effects or other errors accrued between the 10–20'' dithers of the SN exposures. The lower panel plots the RMS residual of the nightly average position against the mean of the entire survey. The RMS expected from the intra-night errors has also been subtracted, leaving an estimate of astrometric errors that are coherent during a night. These are seen to be 2–4 mas RMS, with a tendency to be larger in the E-W direction (red) than N-S (blue).

does not contain proper motions so falls slightly short of our ideal, but these will appear in the DR2 release schedule for April 2018.⁷

Reference stars could also be obtained by repeated ground-based observations to average atmospheric and instrumental effects. We use this approach for a cursory investigation of the potential of reference-catalog interpolation. We extract as a reference catalog the mean positions over all star flat observations of a randomly selected set of stars with mean density of 0.75 arcmin⁻². These “truth” positions are used to interpolate the astrometric distortions for individual exposures. Because our star flat observations span multiple years, the truth positions may also be degraded by proper motions.

We use the SCIKIT-LEARN implementation of Gaussian process (GP) regression to interpolate the errors in the astrometric model on a given exposure. The GP technique requires a kernel specifying the covariance between the error vectors of two stars separated by \mathbf{x} . We take this covariance function to have a white-noise (δ -function) component of amplitude $(4 \text{ mas})^2$ plus a Gaussian with amplitude $(3 \text{ mas})^2$ in the cross-wind direction and $(15 \text{ mas})^2$ in the wind direction. The cross- and along-wind components of \mathbf{x} have independent GP models. The procedure is to:

⁷<http://www.cosmos.esa.int/web/gaia/release>

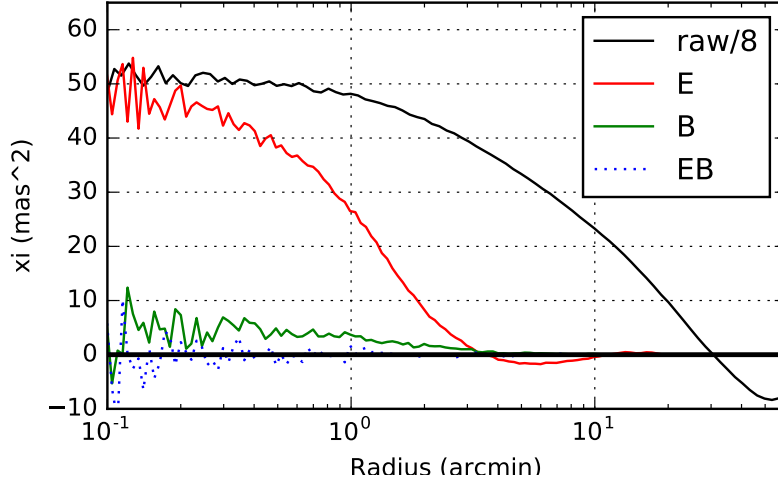


Fig. 17.— The 2-point correlation functions ξ_E, ξ_B , and ξ_x are plotted vs separation both before (“raw”) and after interpolation of the astrometric errors using a reference star set of density 0.75 arcmin^{-2} . The plot shows the mean ξ across $21 \times 30 \text{ s}$ z -band exposures in star-flat epoch 20130829. Note that we plot only ξ_E for the pre-interpolation case (black) since we have found the distortions consistent with pure E -mode behavior, and that the pre-interpolation plot is reduced by a factor of 8 to fit on the same plot. The reduction in ξ from interpolation is dramatic, with correlations at scales above the reference-star density being essentially eliminated.

1. Randomly select a training set of stars at the chosen density and fit the GP model to these.
2. Use the GP to interpolate to the location of each training star, and reject training stars with outlier residuals (*e.g.* high-proper-motion stars).
3. Refit the GP using the retained training stars.
4. Interpolate to the positions the validation set of remaining high- S/N stellar detections.
5. Remove outlying residuals from the validation set.
6. Calculate the 2-point correlation functions of the residuals.

We execute this process for 21 z -band exposures in epoch 20130829, the same set plotted in Figure 11. The mean correlation functions before and after interpolation are plotted in Figure 17. The E mode remains dominant even though the interpolation process is not designed to conserve E/B behavior. As expected, the interpolation reduces ξ_E to negligible levels ($\lesssim 1 \text{ mas}^2$) at scales $> 3'$ where multiple reference stars can contribute to interpolation. The removal of large-scale power reduces the $\xi_E(r)$ at $r \rightarrow 0$ by a factor ≈ 8 from the pre-interpolation value. The average post-interpolation residuals are $< 7 \text{ mas}$ RMS for this epoch, which has typical stochastic signal level ξ_0 . The correlation length of the astrometric errors is reduced to $1'$. One would expect the amplitude of the post-interpolation residuals to decrease with the square root of integration time until the systematic error floor of either the reference catalog or DECam is reached.

This is just an initial investigation: we have attempted to optimize the interpolation procedure neither for accuracy nor speed. Certainly there is improvement to be had through GP kernel optimization or other approaches, including interpolation schemes that exploit the known absence of B modes in the vector distortion field. Doubling the density of reference stars appears to have little effect on the residual amplitude.

9. Conclusions

An astrometric model for DECam with errors near mas level requires terms not only for the polynomial optical “plate solution,” but also contributions from: stray electric fields near the edges in the detector and from “tree ring” impurity fluctuations; lateral color and differential chromatic refraction in the bluer bands; shifts in the CCD positions primarily accrued during focal-plane temperature excursions; and time-variable low-order (cubic) distortions across the FOV from a litany of instrumental and atmospheric effects.

All of these distortions components are determined reliably by fitting a model to stellar positions measured from dithered DECam exposures. External reference catalogs play little role in this process, being needed only to stabilize some large-scale degeneracies such as the overall pixel scale. The WCSFIT software that we created for this purpose is similar to the widely-used SCAMP code in optimizing the parameters of a model to maximize agreement among multiple exposures of the same star. WCSFIT uses simple linearized iterations to minimize a χ^2 , relying on SCAMP or some other code to have produced an initial solution that maps each exposure to $\lesssim 1''$ accuracy. WCSFIT complements SCAMP by: the ability to specify and fit a complex model with many components interlacing their effects among many exposures; enhanced outlier rejection, necessary to achieve precise modelling; and some optimizations for fitting large exposure sets with large numbers of free parameters.

Once this model is fit to an ensemble of DECam exposures, the remaining astrometric errors are dominated by a curl-free stochastic field of atmospheric refraction fluctuations. In a typical 30 s exposure, the stochastic atmospheric distortions are 10–30 mas RMS with coherence length of 4–10' and a strongly anisotropic pattern from wind-blown turbulence. Some nights are much worse than this; unfortunately there is no strong connection between seeing FWHM and astrometric quality.

The atmospheric turbulence averages down with longer exposures or through stacking of residuals on many exposures. Doing so reveals weaker but persistent errors in the astrometric model. Fixed patterns in the devices at 2–4 mas RMS (0.008–0.015 pixel) are dominated by larger residuals on small regions of the device subject to edge effects and mounting structures. These could be tabulated from the device stacks and added to the model if we acquired even more stellar measurements.

Star-flat exposures sequences taken every few months are used to monitor shifts in CCD positions. Using DES supernova-field observations, we determine that the bulk of the observed shifts occurs when DECam’s focal plan warms to room temperature or cools below normal operating temperature. If we apply the CCD shifts measured in the star-flat epochs to the SN data, we find that remaining errors inter-night variation in the solution is 2–4 mas.

The 4'–10' coherence length of the dominant atmospheric distortions suggests that the Gaia reference catalog, with positions and (in the future) proper motions for ≈ 1 star per arcmin² at high Galactic latitude, can be used to constrain and remove the atmospheric pattern (and, trivially, the low-order polynomial distortions). Indeed we find that a trial of Gaussian-process interpolation using reference stars at this density reduces the correlation function $\xi_+(r)$ of errors to < 1 mas² on scales $r > 3'$ and reduce the RMS value at smaller scales to < 7 mas in a 30 s exposure.

The astrometric maps and procedures derived herein will be applied to the DES observations and made available to other users of DECam. We find that errors in the resultant positions are likely to be dominated by (in order of decreasing importance):

- Unavoidable shot noise in the measurement of object centers (for fainter stars).
- Atmospheric turbulence of typical RMS amplitude $(15\text{--}20) \times \sqrt{30/T}$ mas, where T is the exposure time in seconds, and coherence length $\approx 10'$. This amplitude depends on the weather. Given a Gaia catalog with proper motions, the atmospheric field can be measured and interpolated to random locations, leaving residuals $\approx 3\times$ smaller and with coherence length $\approx 1'$.
- Unmodelled night-to-night variations in the DECam astrometric solution at 2–4 mas RMS.
- Up to 2–4 mas RMS additional errors from static detector effects (mounting holes, edge fields) that we do not yet model, but could potentially include given a much larger set of stellar measurement residuals.

We conclude that the DECam astrometric model, with registration to the Gaia catalog, has RMS errors below 10 mas in a typical 30 s exposure, small enough to be negligible for cosmic-shear measurements, and likely to be even smaller in the standard 90-second DES exposure. For a general-use, wide-field instrument like DECam to reach the limit of astrometric accuracy imposed by atmospheric turbulence (with Gaia interpolation gains), the best observing scheme is to dither successive exposures so that the few mas of remaining systematic camera-centered distortions are sampled differently for each exposure of the desired targets. Such a strategy is intrinsic to the DES Wide 5000 deg² survey, so we should expect astrometric catalogs from this survey that are limited by the combination of image shot noise and atmospheric turbulence.

The LSST aims to achieve this goal as well, and the DECam results here show that this should be entirely feasible. LSST has a larger field, shorter exposures, and many more stellar detections to work with. The DECam experience perhaps shows the value of regular star-flat observation sequences. A substantial complication for LSST (as well as other modern wide-field imagers/telescopes such as Hyper Suprime-Cam) is its alt-az mounting and consequent need of an instrument rotator. This introduces a degree of freedom to the optical system absent from the equatorial-mounted Blanco telescope, perhaps greatly increasing the number of constraints that must be analysed to yield a solution valid at all rotator angles. LSST will obtain many more stellar images, so the necessary data will likely exist but pose a bigger computational challenge.

GMB gratefully acknowledges support from grants AST-1311924 and AST-1615555 from the

National Science Foundation, and DE-SC0007901 from the Department of Energy. AAP is supported by the Jet Propulsion Laboratory. Part of the research was carried out at the Jet Propulsion Laboratory, California Institute of Technology, under a contract with the National Aeronautics and Space Administration. We thank Steve Holland and Greg Derylo for help with interpretations of detector and camera behaviors.

The WCSFIT code and subsequent analyses make extensive use of the following excellent public software packages: TMV for linear algebra and TREECORR for fast correlation functions, both by R. M. Jarvis; YAML-CPP by J. Beder for YAML decoding; and CFITSIO by W. Pence, FITSIO by E. Sheldon, and ASTROPY for FITS access in C and Python environments.

Funding for the DES Projects has been provided by the U.S. Department of Energy, the U.S. National Science Foundation, the Ministry of Science and Education of Spain, the Science and Technology Facilities Council of the United Kingdom, the Higher Education Funding Council for England, the National Center for Supercomputing Applications at the University of Illinois at Urbana-Champaign, the Kavli Institute of Cosmological Physics at the University of Chicago, the Center for Cosmology and Astro-Particle Physics at the Ohio State University, the Mitchell Institute for Fundamental Physics and Astronomy at Texas A&M University, Financiadora de Estudos e Projetos, Fundação Carlos Chagas Filho de Amparo à Pesquisa do Estado do Rio de Janeiro, Conselho Nacional de Desenvolvimento Científico e Tecnológico and the Ministério da Ciência, Tecnologia e Inovação, the Deutsche Forschungsgemeinschaft and the Collaborating Institutions in the Dark Energy Survey.

The Collaborating Institutions are Argonne National Laboratory, the University of California at Santa Cruz, the University of Cambridge, Centro de Investigaciones Energéticas, Medioambientales y Tecnológicas-Madrid, the University of Chicago, University College London, the DES-Brazil Consortium, the University of Edinburgh, the Eidgenössische Technische Hochschule (ETH) Zürich, Fermi National Accelerator Laboratory, the University of Illinois at Urbana-Champaign, the Institut de Ciències de l’Espai (IEEC/CSIC), the Institut de Física d’Altes Energies, Lawrence Berkeley National Laboratory, the Ludwig-Maximilians Universität München and the associated Excellence Cluster Universe, the University of Michigan, the National Optical Astronomy Observatory, the University of Nottingham, The Ohio State University, the University of Pennsylvania, the University of Portsmouth, SLAC National Accelerator Laboratory, Stanford University, the University of Sussex, Texas A&M University, and the OzDES Membership Consortium.

The DES data management system is supported by the National Science Foundation under Grant Number AST-1138766. The DES participants from Spanish institutions are partially supported by MINECO under grants AYA2015-71825, ESP2015-88861, FPA2015-68048, SEV-2012-0234, SEV-2012-0249, and MDM-2015-0509, some of which include ERDF funds from the European Union. IFAE is partially funded by the CERCA program of the Generalitat de Catalunya.

REFERENCES

- Abramowitz, M., & Stegun, I. 1965, Handbook of Mathematical Functions, (New York: Dover)
- Anderson, J., Bedin, L. R., Piotto, G., Yadav, R. S., & Bellini, A. 2006, A&A, 454, 1029
- Anderson, J., & King, I. R. 1999, PASP, 111, 1095
- Bertin, E. 2006, Astronomical Data Analysis Software and Systems XV, 351, 112
- Bertin, E., & Arnouts, S. 1996, A&AS, 117, 393
- Bouy, H., Bertin, E., Moraux, E., et al. 2013, A&A, 554, A101
- Flaugher, B., Diehl, H. T., Honscheid, K., et al. 2015, AJ, 150, 150
- The Gaia Collaboration 2016, A&A, 595, A2
- Gruen, D., Bernstein, G. M., Jarvis, M., et al. 2015, Journal of Instrumentation, 10, C05032
- Han, I., & Gatewood, G. D. 1995, PASP, 107, 399
- Heymans, C., Rowe, B., Hoekstra, H., et al. 2012, MNRAS, 421, 381
- LSST Science Collaborations 2009, arXiv:0912.0201
- Magnier, E. A. et al. 2016, arXiv:1612.05242
- Meyers, J. E., & Burchat, P. R. 2015, ApJ, 807, 182
- Plazas, A., & Bernstein, G. 2012, PASP, 124, 1113
- Plazas, A. A., Bernstein, G. M., & Sheldon, E. S. 2014, PASP, 126, 750
- Platais, I., Wyse, R., & Zacharias, N. 2006, PASP, 118, 107
- Press, W. H., Teukolsky, S. A., Vetterling, W. T., & Flannery, B. P. 2003, Numerical Recipes in C++, Cambridge University Press
- Roodman, A., Reil, K., & Davis, C. 2014, Proc. SPIE, 9145, 914516
- Schneider, P., van Waerbeke, L., & Mellier, Y. 2002, A&A, 389, 729.
- Zacharias, N. 1996, PASP, 108, 1135

A. E/B vector field correlation functions

We wish to calculate the correlation functions of the curl-free and divergence-free components of the residual astrometric distortion field $\Delta \mathbf{x}$ on each exposure, given an irregular, noisy sampling of this field by stellar detections. This is closely analogous to the E/B decompositions performed on the spin-2 polarization field of the cosmic microwave background and the spin-2 weak gravitational shear field in many cosmological investigations. We can derive the vector E/B decomposition by a very slight alteration to the shear-field derivation given by [Schneider, van Waerbeke, & Mellier \(2002\)](#).

We start with a 2d vector field $\mathbf{v} = (v_x, v_y)$. It is useful to work with a complex notation $v = v_x + iv_y$ and complex derivatives $\partial = \partial_x + i\partial_y$. We can write an arbitrary vector field as

$$v = \partial\phi(\mathbf{x}), \quad (\text{A1})$$

$$\phi \equiv \phi_E + i\phi_B. \quad (\text{A2})$$

The curl-free E mode of \mathbf{v} is sourced by ϕ_E and the divergence-free B mode by ϕ_B .

The 2-point correlation functions of \mathbf{v} at separation vector \mathbf{r} are best posed in terms of the quantity $v_{\parallel} + iv_{\perp} = ve^{-i\beta}$, where β is the position angle of \mathbf{r} . We define

$$\xi_+(\mathbf{r}) = \xi_+(r, \beta) = \left\langle v(\mathbf{x})e^{-i\beta} \left[v(\mathbf{x} + \mathbf{r})e^{-i\beta} \right]^* \right\rangle \quad (\text{A3})$$

$$\xi_-(r, \beta) + i\xi_{\times}(r, \beta) = \left\langle v(\mathbf{x})e^{-i\beta} v(\mathbf{x} + \mathbf{r})e^{-i\beta} \right\rangle \quad (\text{A4})$$

Taking $\tilde{\phi}(\mathbf{k})$ to be the Fourier transform of ϕ , and the generation of ϕ to be a stationary stochastic process, we define the power spectra via

$$\left\langle \tilde{\phi}_E(\mathbf{k}_1)\tilde{\phi}_E^*(\mathbf{k}_2) \right\rangle = (2\pi)^2\delta(\mathbf{k}_1 - \mathbf{k}_2)P_{EE}(\mathbf{k}_1) \quad (\text{A5})$$

$$\left\langle \tilde{\phi}_E(\mathbf{k}_1)\tilde{\phi}_B^*(\mathbf{k}_2) \right\rangle = (2\pi)^2\delta(\mathbf{k}_1 - \mathbf{k}_2)P_{EB}(\mathbf{k}_1)$$

$$\left\langle \tilde{\phi}_B(\mathbf{k}_1)\tilde{\phi}_B^*(\mathbf{k}_2) \right\rangle = (2\pi)^2\delta(\mathbf{k}_1 - \mathbf{k}_2)P_{BB}(\mathbf{k}_1).$$

P_{EB} must be real if the vector field statistics are invariant under 180° rotation, so we will assume this is true. The real part will vanish as well if the process generating \mathbf{v} is invariant under parity flips. We will leave the real part as a free parameter.

By propagating the derivatives in Equation (A1) through a Fourier transform we can express the correlation functions (A3) and (A4) as

$$\xi_+(r, \beta) = \int d\alpha \int k dk |k^2| e^{ikr \cos(\alpha-\beta)} [P_{EE}(k, \alpha) + P_{BB}(k, \alpha)] \quad (\text{A6})$$

$$\xi_-(r, \beta) + i\xi_{\times}(r, \beta) = \int d\alpha \int k dk |k^2| e^{-ikr \cos(\alpha-\beta)} e^{2i(\alpha-\beta)} [P_{EE}(k, \alpha) - P_{BB}(k, \alpha) + 2iP_{EB}(k, \alpha)] \quad (\text{A7})$$

where α is the position angle of the wavevector \mathbf{k} . Even though the atmospheric distortions are anisotropic, we will concern ourselves only with the angle-average quantities $\xi_+(r) = \langle \xi_+(r, \beta) \rangle_\beta$, and the corresponding angle-averaged power spectra $P_{EE}(k)$, etc. If we average the preceding equations over β , Bessel’s first integral yields

$$\xi_+(r) = 2\pi \int k dk k^2 J_0(kr) [P_{EE}(k) + P_{BB}(k)] \quad (\text{A8})$$

$$\xi_-(r) = -2\pi \int k dk k^2 J_2(kr) [P_{EE}(k) - P_{BB}(k)] \quad (\text{A9})$$

$$\xi_\times(r) = -4\pi \int k dk k^2 J_2(kr) P_{EB}(k). \quad (\text{A10})$$

The last equation tells us that ξ_\times is produced purely by EB power. Let us define pure-E and pure-B quantities

$$\xi_{E,B}(r) \equiv 2\pi \int k dk k^2 J_0(kr) P_{EE,BB}(k) \quad (\text{A11})$$

$$= \frac{1}{2} \left\{ \xi_+(r) \mp \int r dr J_0(r) \int r' dr' J_2(r') \xi_-(r') \right\} \quad (\text{A12})$$

where the last line combines Equation (A8) with the order-2 Hankel Transform of Equation (A9). After making use of identities 9.1.27 and 11.4.42 from [Abramowitz & Stegun \(1965\)](#), this can be converted to

$$\xi_{E,B}(r) = \frac{1}{2} \left\{ \xi_+(r) \pm \left[\xi_-(r) - 2 \int_r^\infty dr' \frac{1}{r'} \xi_-(r') \right] \right\}. \quad (\text{A13})$$

Equations (A10) and (A13) allow us to produce measures of pure E, B, and cross-EB power from 2-point correlations constructed from all pairs of detections in a given exposure. In [Figure 18](#) we plot ξ_E and ξ_B inferred for the astrometric residuals in each of 20 consecutive star-flat exposures (after projecting out a cubic polynomial function of field coordinates from each exposure). It is clear that the astrometric residuals are indeed dominated by E modes, *e.g.* curl-free. [Figure 11](#) plots the mean of ξ_E , ξ_B , and ξ_\times in another set of exposures, confirming that any divergence modes are very small. In further analysis we assumed $\xi_B = 0$ such that we can more simply take $\xi_E = \xi_+$.

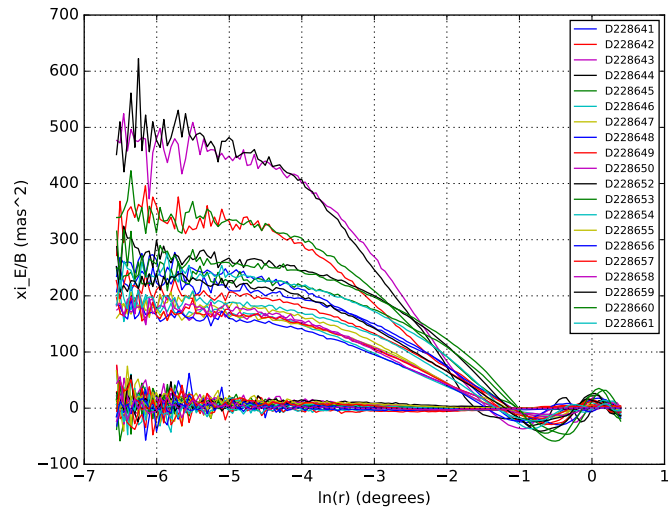


Fig. 18.— The ξ_E (upper curves) and ξ_B (lower set) derived via Equation (A13) for each of a series of exposures, demonstrating that the astrometric errors are dominated by a curl-free vector field, as expected from atmospheric refraction fluctuations.